JPn Neuroscience

The Journal of Physiology

J Physiol 592.10 (2014) pp 2097–2118

Greater excitability and firing irregularity of tufted cells underlies distinct afferent-evoked activity of olfactory bulb mitral and tufted cells

Shawn D. Burton and Nathaniel N. Urban

Department of Biological Sciences, Center for the Neural Basis of Cognition, Carnegie Mellon University, Pittsburgh, PA 15213, USA

Key points

- The two classes of principal neurons in the mammalian main olfactory bulb, mitral and tufted cells, respond with different firing latencies and rates to afferent-evoked input; how these differences in activity arise is incompletely understood.
- Tufted cells receive stronger afferent-evoked excitation than mitral cells, but this difference alone is insufficient to account for the greater afferent-evoked firing in tufted *versus* mitral cells.
- Mitral and tufted cells exhibit significant intrinsic functional differences; compared to mitral cells, tufted cells fire action potentials with shorter durations and faster afterhyperpolarizations and exhibit twofold greater firing rate–current curve gains and peak rates.
- Tufted cells exhibit diverse firing modes, including tonic firing and irregular stuttering, and on average fire more irregularly than mitral cells.
- Collectively, stronger afferent excitation, greater intrinsic excitability and more irregular firing in tufted cells combine to drive distinct responses of mitral and tufted cells to sensory input.

Abstract Mitral and tufted cells, the two classes of principal neurons in the mammalian main olfactory bulb, exhibit morphological differences but remain widely viewed as functionally equivalent. Results from several recent studies, however, suggest that these two cell classes may encode complementary olfactory information in their distinct patterns of afferent-evoked activity. To understand how these differences in activity arise, we have performed the first systematic comparison of synaptic and intrinsic properties between mitral and tufted cells. Consistent with previous studies, we found that tufted cells fire with higher probability and rates and shorter latencies than mitral cells in response to physiological afferent stimulation. This stronger response of tufted cells could be partially attributed to synaptic differences, as tufted cells received stronger afferent-evoked excitation than mitral cells. However, differences in intrinsic excitability also contributed to the differences between mitral and tufted cell activity. Compared to mitral cells, tufted cells exhibited twofold greater excitability and peak instantaneous firing rates. These differences in excitability probably arise from differential expression of voltage-gated potassium currents, as tufted cells exhibited faster action potential repolarization and afterhyperpolarizations than mitral cells. Surprisingly, mitral and tufted cells also showed firing mode differences. While both cell classes exhibited regular firing and irregular stuttering of action potential clusters, tufted cells demonstrated a greater propensity to stutter than mitral cells. Collectively, stronger afferent-evoked excitation, greater intrinsic excitability and more irregular firing in tufted cells can combine to drive distinct responses of mitral and tufted cells to afferent-evoked input.

(Received 13 December 2013; accepted after revision 4 March 2014; first published online 10 March 2014)
Corresponding author N. N. Urban: Carnegie Mellon University, Biological Sciences, 4400 Fifth Ave., Mellon Institute, Pittsburgh, PA 15213, USA. Email: nurban@cmu.edu

DOI: 10.1113/jphysiol.2013.269886

Abbreviations AHP, afterhyperpolarization; ANOVA, analysis of variance; C_m, membrane capacitance; CV_{ISI}, coefficient of variation of interspike intervals; EPL, external plexiform layer; ETC, external tufted cell; FI, firing rate-current; FWHM, full action potential width at half-maximal amplitude; GC, granule cell; GL, glomerular layer; ISI, interspike interval; LLD, long-lasting depolarization; MC, mitral cell; MCL, mitral cell layer; MOB, main olfactory bulb; MRR, molecular receptive range; ONL, olfactory nerve layer; OSN, olfactory sensory neuron; PGC, periglomerular cell; R_{input}, input resistance; R_s, series resistance; SEM, standard error of the mean; τ_m, membrane time constant; $T_{AHP\ 50\%}$, afterhyperpolarization duration; TC, tufted cell; V_m, membrane potential; V_{rest}, resting membrane potential; $V_{threshold}$, action potential threshold.

Introduction

Mitral cells (MCs) and tufted cells (TCs), the two classes of principal neurons in the mammalian main olfactory bulb (MOB), are distinguished by their distinct morphology and axonal projections, but whether they are also functionally different remains controversial (for review, see Macrides *et al.* 1985; Mori & Sakano, 2011). Results from several recent studies, however, suggest that these two cell classes may encode complementary olfactory information in distinct patterns of odour-evoked activity. Compared to MCs, TCs respond to lower odour concentrations (Igarashi *et al.* 2012; Kikuta *et al.* 2013), exhibit greater odour concentration invariance in their activity (Fukunaga *et al.* 2012; Igarashi *et al.* 2012), fire earlier in the sniff cycle (Fukunaga *et al.* 2012; Igarashi *et al.* 2012) and exhibit higher odour-evoked firing rates (Nagayama *et al.* 2004; Griff *et al.* 2008). Differentiating what olfactory information is encoded by MCs *vs.* TCs will first require understanding the origin of their distinct odour-evoked activity.

The differences in odour-evoked activity between MCs and TCs may result from differences in synaptic properties, intrinsic biophysical properties or both. Synaptic differences are likely to be a critical factor, as TCs receive more effective monosynaptic input from olfactory sensory neurons (OSNs) (Gire *et al.* 2012) and weaker lateral inhibition (Ezeh *et al.* 1993; Christie *et al.* 2001; Phillips *et al.* 2012) than MCs. Whether these synaptic differences are sufficient to explain the differences in odour-evoked activity between MCs and TCs has not been examined, however. Furthermore, no study to date has investigated whether the two classes of MOB principal neurons differ in their intrinsic biophysical properties. Indeed, most studies of 'tufted cell' physiology have focused exclusively on external tufted cells (ETCs), a distinct population of rhythmically bursting glutamatergic interneurons (e.g. see: Hayar *et al.* 2004; Liu & Shipley, 2008; De Saint Jan *et al.* 2009) responsible for driving the indirect, long-lasting depolarization (LLD) of MCs and TCs following direct OSN input (De Saint Jan *et al.* 2009; Gire & Schoppa, 2009; Najac *et al.* 2011; Gire *et al.* 2012).

Equally important to the strength and timing of odour-evoked activity is the temporal pattern of action potentials evoked by sensory input (Schaefer & Margrie, 2007). Multicellular *in vivo* recordings have established that olfactory experience evokes precise, odour-specific spatiotemporal patterns of firing in principal neurons across the MOB (for review, see Friedrich, 2006; Bathellier *et al.* 2010). Diversity in principal neuron firing modes is a critical factor contributing to the encoding of stimulus-specific information (Padmanabhan & Urban, 2010; Angelo & Margrie, 2011; Tripathy *et al.* 2013) and regulation of neuronal synchrony (Burton *et al.* 2012) in these population activity patterns. *In vivo* recordings have shown that a subset of MOB principal neurons exhibit regular, tonic firing characterized by low interspike interval (ISI) coefficients of variation (CV_{ISI}), while other principal neurons exhibit irregular firing of action potential clusters (i.e. 'stuttering') with high CV_{ISI} (Buonviso *et al.* 2003; Margrie & Schaefer, 2003; Schaefer *et al.* 2006; Bathellier *et al.* 2008; Cury & Uchida, 2010; Carey & Wachowiak, 2011; Shusterman *et al.* 2011). Systematic investigation *in vitro* has confirmed that MC populations exhibit both tonic and stuttering firing modes and has provided some detail about the mechanisms by which these firing modes are generated (Chen & Shepherd, 1997; Desmaisons *et al.* 1999; Friedman & Strowbridge, 2000; Balu *et al.* 2004; Schaefer *et al.* 2006; Padmanabhan & Urban 2010; Angelo & Margrie, 2011; Fadool *et al.* 2011; Tucker *et al.* 2013). Equivalent investigation of TC firing modes is currently lacking and will be critical in understanding how TC activity contributes to MOB population activity patterns.

Here, we describe mechanisms by which MCs and TCs may encode distinct olfactory information. We first demonstrate that the differential firing responses of MCs and TCs to afferent-evoked input observed *in vivo* are maintained *in vitro*, facilitating more detailed exploration of their origin. Voltage-clamp recordings confirm that TCs receive stronger afferent-evoked excitation than MCs. Surprisingly, however, this synaptic difference is poorly correlated with the differences between MC and TC afferent-evoked firing rates. To identify other factors contributing to the different afferent-evoked firing rates of MCs and TCs, we thus perform the first systematic comparison of MC and TC biophysical properties. Critically, TCs are intrinsically twice as excitable as MCs, and this difference in excitability provides a better prediction of the distinct afferent-evoked firing rates of

MCs and TCs than the strength of their afferent-evoked excitation. Our results thus suggest that both synaptic and, in particular, intrinsic cellular properties underlie the greater odour-evoked TC firing rates observed *in vivo*. We additionally find that TCs exhibit both tonic and stuttering firing modes, but fire significantly more irregularly than MCs, emphasizing the important contribution of high-frequency action potential clusters to TC coding. The amplitude of membrane potential sag mediated by hyperpolarization-activated currents directly correlates with firing regularity in TCs, similar to MCs (Angelo & Margrie, 2011), but does not directly predict the greater firing irregularity of TCs *vs.* MCs. Collectively, our results thus identify several key functional differences through which the two classes of MOB principal neurons may transform convergent sensory input into complementary olfactory information.

Methods

Ethical approval

All experiments were completed in compliance with the guidelines established by the Institutional Animal Care and Use Committee of Carnegie Mellon University.

Animals

Multiple strains of mice with the C57BL/6 background were used in this study with no difference in results between strains (data not shown). Strains included wild type C57BL/6 ($n = 8$), Thy1-YFP-G ($n = 14$) (Feng *et al.* 2000), V2R-GFP ($n = 1$) (Del Punta *et al.* 2002) and M72-GFP ($n = 15$) (Potter *et al.* 2001).

Slice preparation

Postnatal day 13–20 mice of both sexes were anaesthetized with isoflurane and decapitated into ice-cold oxygenated dissection solution containing (in mM): 125 NaCl, 25 glucose, 2.5 KCl, 25 $NaHCO_3$, 1.25 NaH_2PO_4, 3 $MgCl_2$ and 1 $CaCl_2$. Brains were rapidly isolated and acute horizontal, sagittal and oblique slices (310″ μm thick) of the MOB were prepared using a vibratome (VT1200S; Leica, Nussloch, Germany, or 5000 mz-2; Campden, Lafayette, IN, USA). Slices recovered for 15–30 min in ∼37°C oxygenated Ringer solution that was identical to the dissection solution except for lower Mg^{2+} concentrations (1 mM $MgCl_2$) and higher Ca^{2+} concentrations (2 mM $CaCl_2$). Slices were then stored in room temperature oxygenated Ringer solution until recording.

Cell classification

MOB principal neurons were identified by: (1) large cell body size, (2) cell body position within the MC layer (MCL) or external plexiform layer (EPL), (3) the presence of an apical dendrite projecting toward the glomerular layer (GL) and (4) the presence of at least one lateral dendrite, consistent with classical classification schema (e.g. see: Macrides & Schneider, 1982; Mori *et al.* 1983; Kishi *et al.* 1984). Principal neurons were classified as MCs if >50% of their cell body resided within the MCL. Principal neurons with cell bodies located only partially within the MCL (i.e. <50% of the cell body) represent 'displaced MCs' (Mori *et al.* 1983; Kishi *et al.* 1984) and 'internal TCs' (Ghosh *et al.* 2011; Igarashi *et al.* 2012), and were not targeted for recording due to their ambiguous identity as MCs or TCs without full axonal tracing. Principal neurons with cell bodies residing completely within the EPL (i.e. 0% within the MCL) were classified as TCs. Under this classification scheme, our MC dataset included clear examples of both type I (e.g. see: supplementary Fig. S1, mitral cells 02, 04, 06, 07, 18) and type II (e.g. see: Fig. S1, mitral cells 01, 11, 13, 32, 35) MCs that extend their lateral dendrites into the deep and superficial EPL, respectively (Orona *et al.* 1984), as well MCs with more ambiguous lateral dendrite depths (e.g. see: Fig. S1, mitral cells 08, 19, 20, 21, 31). Furthermore, our resulting TC dataset included cells ranging from deep (e.g. see: Fig. S2, tufted cells 06, 07, 09) to superficial (e.g. see: Fig. S2, tufted cells 12, 26, 27) TCs. Importantly, none of the cells included in the TC dataset exhibited the rhythmic bursting characteristic of ETCs (e.g. see: Hayar *et al.* 2004; Liu & Shipley, 2008; De Saint Jan *et al.* 2009).

Electrophysiology

Slices were continuously superfused with 37°C oxygenated Ringer solution. Cells were visualized using infrared differential interference contrast video microscopy. Whole-cell recordings were made from individual cells using electrodes filled with (in mM) 120 potassium gluconate, 2 KCl, 10 Hepes, 10 sodium phosphocreatine, 4 Mg-ATP, 0.3 Na_3GTP, 0–0.2 EGTA, 0–0.25 Alexa Fluor 594 (Life Technologies, Carlsbad, CA, USA) and 0.2% Neurobiotin (Vector Labs, Burlingame, CA, USA). The liquid junction potential was 12–14 mV and was not corrected for. Cell morphology was reconstructed under a 100× oil-immersion objective and analysed with Neurolucida (MicroBrightField, Inc., Williston, VT, USA). In all reconstructed cells shown, the MCL is bracketed by light grey contours and the division between the GL and EPL is shown by a dark grey contour. All cells included in this dataset exhibited spontaneous LLDs (Carlson *et al.* 2000) and/or intact apical tufts upon reconstruction. A minority of MCs sent a second, thin dendrite to co-terminate with their main apical dendritic tuft in the glomerular layer. These secondary glomerular projections were not included in our quantification of cell morphologies. Data were low-pass filtered at 4 kHz and digitized at 10 kHz using a MultiClamp 700A amplifier (Molecular Devices,

Sunnyvale, CA, USA) and an ITC-18 acquisition board (Instrutech, Mineola, NY, USA) controlled by custom software written in Igor Pro (WaveMetrics, Lake Oswego, OR, USA).

For extracellular stimulation, a monopolar glass electrode was filled with Ringer solution and connected to a stimulus isolation unit (World Precision Instruments, Sarasota, FL, USA) controlled by transistor–transistor logic pulses from the ITC-18 acquisition board. Stimulus intensity was adjusted until all-or-nothing LLDs (either following or occluding direct monosynaptic OSN input) were reliably (∼95% success rate) evoked on each trial. These stimulus intensities and the position of the stimulation electrode (olfactory nerve layer (ONL) *vs.* GL) differs from our previous study examining MC *vs.* TC response latencies to minimal glomerulus stimulation (Giridhar & Urban, 2012). For conciseness, we use the phrase 'afferent-evoked' to refer to the activity and synaptic input of MCs and TCs arising from the combined direct monosynaptic OSN input and indirect polysynaptic ETC input (i.e. the glomerular LLD) evoked by activating OSN afferents in the ONL.

For measurements of action potential properties (except for afterhyperpolarization (AHP) duration; see below), pipette capacitance was neutralized and series resistance (R_s) was stringently minimized (MC: 11.7 ± 1.5 MΩ, range: 8.4–13.0 MΩ, $n = 10$; TC: 13.1 ± 1.5 MΩ, range: 9.6–15.5 MΩ, $n = 12$) and compensated for using the MultiClamp Bridge Balance operation. For measurements of afferent-evoked activity and input, pipette capacitance was neutralized and R_s (MC: 20.0 ± 3.9 MΩ, range: 16.4–26.7 MΩ, $n = 6$; TC: 15.8 ± 3.8 MΩ, range: 12.6–22.9 MΩ, $n = 7$) was compensated for using the MultiClamp Bridge Balance operation in current clamp and compensated for ≥60% in voltage clamp. R_s was maintained below 40 MΩ (MC: 20.1 ± 7.4 MΩ, range: 8.4–32.5 MΩ, $n = 35$; TC: 22.3 ± 9.6 MΩ, range: 9.6–39.0 MΩ, $n = 28$) and compensated for using the MultiClamp Bridge Balance operation for all other measurements, including AHP duration ($T_{AHP\ 50\%}$), which did not significantly vary with R_s in our recordings. Electrode resistance was comparable for TC and MC recordings (MC: 6.3 ± 1.0 MΩ, range: 4.7–8.9 MΩ, $n = 41$; TC: 6.7 ± 1.1 MΩ, range: 4.7–8.6 MΩ, $n = 35$). Resting membrane potential (V_{rest}) was determined immediately after break in. For measurements of action potential and spike train properties, current was injected to normalize V_m to −58 mV and ionotropic synaptic transmission was blocked by 6-cyano-7-nitroquinoxaline-2,3-dione (CNQX, 10 μM), DL-2-amino-5-phosphonopentanoic acid (DL-APV, 50 μM) and gabazine (10 μM) (with the exception of Fig. 3 where ionotropic synaptic transmission was not blocked) after determination of V_{rest} and the presence of spontaneous LLDs. For measurements of afferent-evoked spiking, current was injected to normalize V_m to −50 mV. Voltage clamp recordings were performed at −60 mV. Afferent-evoked activity was recorded in response to a train of extracellular stimulation pulses delivered to the ONL and averaged over 3–10 trials per stimulation frequency, with an inter-trial interval of 20 s.

Data analysis

Afferent-evoked firing rates were calculated by dividing the total number of action potentials evoked in each stimulation cycle by the duration of each stimulation cycle. Afferent-evoked firing latencies were calculated as the time of afferent stimulation to the time of the first action potential (on suprathreshold trials). These latencies were then normalized by the total duration of the stimulation cycle and linearly converted to phase (measured in radians). For analysis of afferent-evoked synaptic currents, the rapid and delayed current peaks and charge transfer were calculated after subtracting the baseline current (measured as the current 10 ms preceding the stimulation). Charge transfer was calculated by integrating currents across the duration of each stimulation cycle (e.g. across each 250 ms window following afferent stimulation at 4 Hz). On some stimulation cycles in voltage-clamped TCs, the short-latency afferent-evoked current was strong enough to generate an escaped action potential; these trials were not considered in our analysis.

Membrane time constant (τ_m), input resistance (R_{input}) and capacitance (C_m) were calculated from hyperpolarizing step current injections as previously described (Golowasch *et al.* 2009). Sag amplitude was measured as in previously published methods (Angelo & Margrie, 2011). Briefly, cells were injected with a series of 2 s hyperpolarizing steps ranging from 0 to −300 pA in steps of −50 pA. The sag amplitude of the cell was then calculated as the initial response subtracted from the steady state response for whichever current injection yielded a steady state response closest to −90 mV. For cells in which membrane potential reached a minimum and then depolarized until the end of the step current injection (e.g. see Fig. 7*B*, *D*), the initial response was calculated as the minimum voltage reached during the step current injection. For cells in which membrane potential continued to hyperpolarize throughout the duration of the step current injection (e.g. see Fig. 7*A*, *C*), the initial response was calculated as the voltage at 100 ms after the beginning of the hyperpolarizing current injection (the time at which cells with positive sag typically reached their minimum). Firing rate–current (FI) curves were calculated from injections of 2 s depolarizing steps ranging from 0 to 300 pA in steps of 50 pA, consistent with the physiological range of LLD amplitudes observed (Fig. 2; Carlson *et al.* 2000; Gire *et al.* 2012). Spike times and action potential threshold ($V_{threshold}$) were measured by defining the onset of an action potential as the time at which the

voltage derivative exceeded 20 mV ms^{-1}. For each cell, action potential properties were calculated from the first action potential evoked by the weakest suprathreshold input (i.e. 'rheobase'). Action potential amplitude was measured as the difference between the voltage at action potential onset and peak. This amplitude was then used to calculate the full action potential width at half-maximal amplitude (FWHM). Slopes of action potential rising and falling phases were calculated as the respective maximum and minimum slopes achieved during an action potential. AHP amplitude was calculated as the minimum voltage reached within 10 ms after an action potential subtracted from $V_{threshold}$. $T_{AHP\ 50\%}$ was calculated by measuring the time of AHP start (when the action potential falling phase reached $V_{threshold}$) to the time at which the AHP had decayed to 50% of its maximal amplitude. The peak instantaneous firing rate was calculated as the inverse of the minimum ISI recorded during step current injections. FI curve gain was calculated as the maximum linear slope of the FI relationship. Spike latencies were measured from the time of step current onset to the first spike time at rheobase input.

Measurements of afferent-evoked activity were compared between MCs and TCs (and across stimulation cycles) using a two-way analysis of variance (ANOVA) with *post hoc* Tukey's test. Measurements of firing regularity (i.e. CV_{ISI}) were compared between MCs and TCs (and across step current amplitudes) using a two-way ANOVA with *post hoc* Tukey's test. All other statistical comparisons were made using linear regression and the non-parametric Wilcoxon rank sum test. Values are reported as mean ± SD unless otherwise noted. All analyses were performed in MATLAB (MathWorks, Natick, MA, USA).

Results

MCs and TCs exhibit different afferent-evoked activity *in vitro*

Previous studies have explored the firing response of MCs to the combined monosynaptic OSN input and polysynaptic ETC input (i.e. the glomerular LLD) evoked by afferent stimulation *in vitro* (e.g. see: Carlson *et al.* 2000; Schoppa, 2006; De Saint Jan *et al.* 2009; Gire & Schoppa, 2009; Najac *et al.* 2011; Gire *et al.* 2012; Shao *et al.* 2012, 2013) but have not examined the equivalent afferent-evoked firing response of TCs *in vitro*. Thus, whether the differential afferent-evoked MC *vs.* TC activity observed *in vivo* is maintained *in vitro* is not known. Critically, the maintenance of *in vivo* MOB activity patterns in acute slices is not guaranteed, given the substantial excitatory (Balu *et al.* 2007; Boyd *et al.* 2012; Markopoulos *et al.* 2012), inhibitory (Gracia-Llanes *et al.* 2010; Nunez-Parra *et al.* 2013) and neuromodulatory (Petzold *et al.* 2009; Devore & Linster 2012) centrifugal input to the MOB that is disrupted in acute slices. Such centrifugal input can influence not only the strength of afferent input (for review, see McGann, 2013) but also may regulate levels of tonic inhibition in the MOB (e.g. see Labarrera *et al.* 2013), which may differentially influence MC *vs.* TC afferent-evoked activity *in vivo*. Thus, to explore the mechanisms underlying differential afferent-evoked MC *vs.* TC activity observed *in vivo*, we first examined whether similar afferent-evoked activity patterns are maintained *in vitro*.

To simulate physiological sniff-coupled afferent-evoked input (Cang & Isaacson, 2003; Margrie & Schaefer, 2003; Schaefer *et al.* 2006; Phillips *et al.* 2012), we stimulated the ONL with a train of five 100 μs constant current pulses (10–100 μA) at 2, 4 and 8 Hz while recording from individual MCs and TCs located slightly caudal to the extracellular stimulation electrode (Fig. 1*A*–*C*). These stimulation frequencies were selected to explore the response of MOB principal neurons to both passive respiratory and active sniffing frequencies of rodents (for review, see Wachowiak, 2011). For each recording, the stimulus intensity was increased until the first pulse of each train reliably (∼95% success rate) evoked afferent-evoked input in the form of an all-or-nothing LLD (Carlson *et al.* 2000; Gire & Schoppa, 2009) and then kept constant for all trials.

Compared to MCs, TCs exhibited higher afferent-evoked firing rates on suprathreshold trials (Fig. 1*D*), were more likely to fire on any given trial (Fig. 1*E*) and fired earlier in the stimulation cycle (Fig. 1*F*) across all stimulation frequencies examined. Indeed, across all trials and stimulation cycles (including both sub- and suprathreshold cycles), TC firing rates were on average 4.4, 3.8 and 2.9 times greater than MC firing rates across 2, 4 and 8 Hz stimulation frequencies, respectively. These results agree with classical studies examining the *in vivo* response of MCs and TCs to a single ONL stimulation pulse (Schneider & Scott, 1983; Wellis *et al.* 1989; Ezeh *et al.* 1993). Furthermore, these results parallel analogous studies examining the odour-evoked activity of MCs and TCs (Nagayama *et al.* 2004; Griff *et al.* 2008; Igarashi *et al.* 2012; Fukunaga *et al.* 2012; Kikuta *et al.* 2013). In particular, the 2- to 3-fold greater afferent-evoked firing rates observed in TCs relative to MCs on suprathreshold trials *in vitro* (Fig. 1*D*) closely matches the 2- to 3-fold greater odour-evoked firing rates observed in TCs relative to MCs *in vivo* (Nagayama *et al.* 2004). Likewise, the shorter afferent-evoked firing latencies of TCs relative to MCs *in vitro* agree with the shorter odour-evoked firing latencies of TCs relative to MCs *in vivo*. Interestingly, however, the ∼25–50 ms difference in *in vitro* latencies (Fig. 1*F*) is consistently less than the ∼150–200 ms difference in odour-evoked latencies at low odour concentrations (Fukunaga *et al.* 2012; Igarashi *et al.* 2012). This discrepancy in absolute latencies

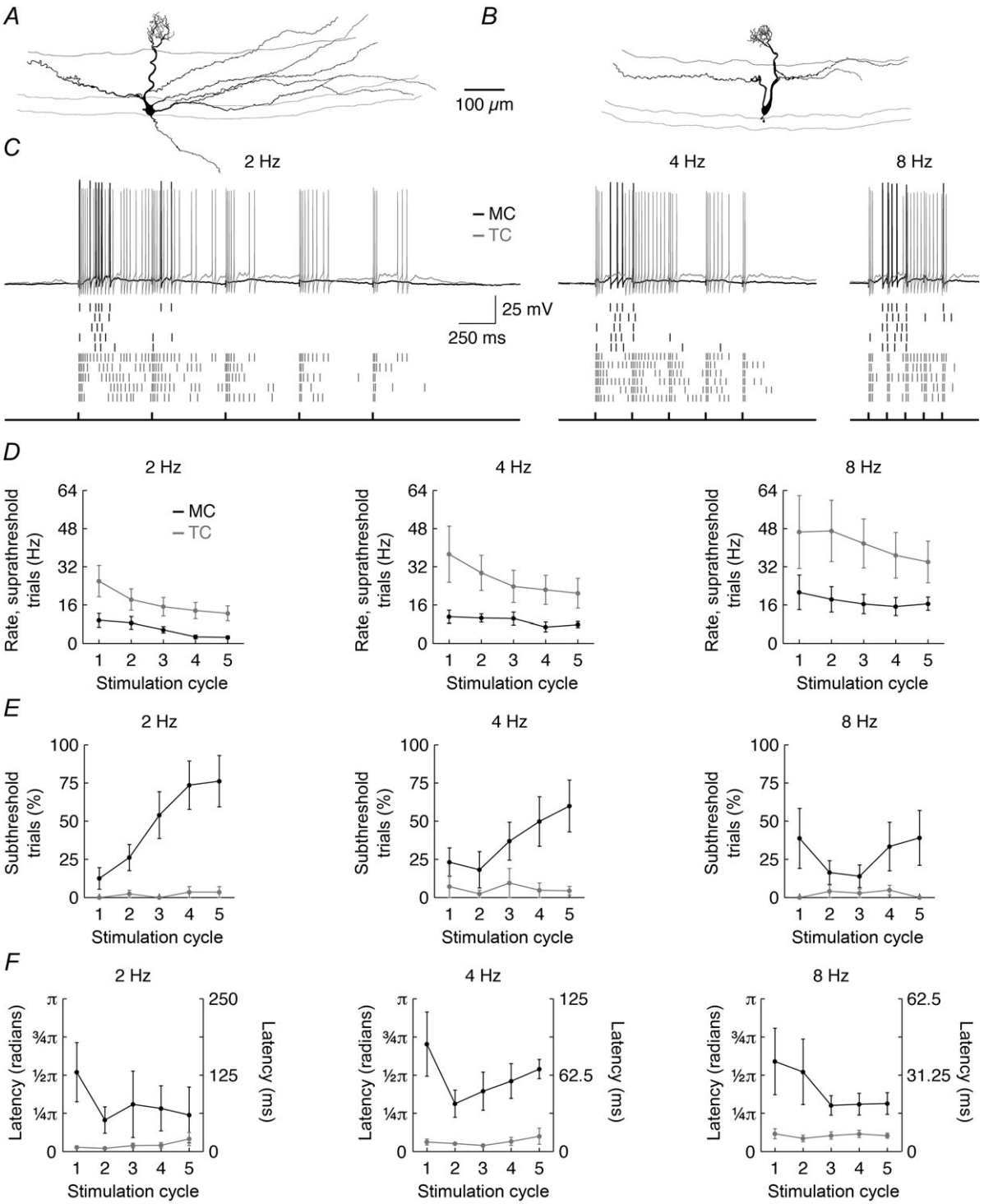

Figure 1. Differential responses of MCs and TCs to afferent input are maintained *in vitro*
A and *B*, morphology of a representative MC (*A*) and TC (*B*). *C*, example afferent-evoked firing response (top) of the representative cells shown in *A* and *B* in response to 2, 4 and 8 Hz ONL stimulation. Raster plots (middle) show the firing response across successive trials (first row for each cell shows the example spiking response plotted at the top). Timing of ONL stimulation is plotted at the bottom. *D*, mean afferent-evoked firing rate on suprathreshold trials was significantly greater in TCs than in MCs (2 Hz: $P = 6.9 \times 10^{-5}$; 4 Hz: $P = 4.1 \times 10^{-5}$; 8 Hz: $P = 2.0 \times 10^{-4}$). *F*, percentage of subthreshold trials was significantly higher in MCs than in TCs (2 Hz: $P = 5.2 \times 10^{-10}$; 4 Hz: $P = 6.1 \times 10^{-6}$; 8 Hz: $P = 8.8 \times 10^{-5}$). *G*, first-spike latency on suprathreshold trials was significantly shorter in TCs than in MCs (2 Hz: $P = 5.5 \times 10^{-5}$; 4 Hz: $P = 6.0 \times 10^{-10}$; 8 Hz: $P = 2.0 \times 10^{-6}$). Data in *D*–*G* were recorded from six MCs and seven TCs.

can be partially attributed to differences in stimulation methods (synchronous ONL stimulation *vs.* asynchronous odour-binding kinetics), and also to potential differences in the inhibitory tone of the MOB circuit under *in vitro* and *in vivo* conditions, as Fukunaga *et al.* (2012) have elegantly demonstrated that interruption of fast inhibition disrupts differences in odour-evoked latencies between MCs and TCs.

Collectively, our results thus confirm that the acute MOB slice provides a viable preparation for exploring mechanisms driving distinct MC *vs.* TC afferent-evoked activity – in particular, differences in afferent-evoked firing rates. Moreover, these results demonstrate that centrifugal input is not necessary to generate stronger afferent-evoked activity in TCs compared to MCs, suggesting that centrifugal input may regulate temporal aspects of olfactory processing predominantly downstream of MC/TC transformation of afferent input (Oswald & Urban, 2012*a*). Intriguingly, the increasing fraction of subthreshold responses from MCs (but not TCs) across sequential stimulation cycles (Fig. 1*E*) also predicts that TC firing may contribute more to total MOB activity patterns than MC firing during prolonged odour exposures. This finding also provides indirect evidence supporting the hypothesis that MCs receive greater levels of afferent-evoked (probably periglomerular cell (PGC)-mediated) inhibition than TCs (Fukunaga *et al.* 2012; see Discussion).

Differences in afferent-evoked excitation and excitability between MCs and TCs contribute to differences in afferent-evoked firing rates

Gire *et al.* (2012) have recently demonstrated that TCs receive stronger afferent-evoked excitation than MCs following brief electrical ONL or optogenetic OSN stimulation. This previous study, however, did not assess whether this differential afferent-evoked excitation is sufficient to explain the stronger afferent-evoked firing response of TCs compared to MCs. To address this question, we again stimulated the ONL but voltage clamped MCs and TCs at −60 mV (i.e. near the reversal potential for Cl^-) to record their excitatory synaptic input. In agreement with Gire *et al.* (2012), we observed significantly larger synaptic currents in TCs than in MCs (Fig. 2). Specifically, ONL stimulation transferred on average 1.9, 1.8 and 2.1 times more charge to TCs than MCs across 2, 4 and 8 Hz stimulation frequencies, respectively (Fig. 2*D*). The greater charge transferred to TCs compared to MCs was predominantly due to a significantly larger short-latency, rapidly decaying current in TCs than in MCs (Fig. 2*E*), consistent with an effectively stronger monosynaptic connection of OSNs to TCs than to MCs (Gire *et al.* 2012). TCs additionally demonstrated modestly larger delayed peak currents (>30 ms after stimulation) driven by the glomerular LLD (Fig. 2*F*). Critically, these synaptic differences are not due to differences in apical dendrite length and filtering, as dual somatodendritic recordings have established that LLD events are propagated to the soma of MOB principal neurons with minimal attenuation (Carlson *et al.* 2000; Gire *et al.* 2012).

TCs thus receive stronger afferent-evoked excitation than MCs. However, this difference in excitation is smaller than the differences observed in afferent-evoked MC *vs.* TC firing rates (compare Figs 1 and 2). The greater TC firing rates may arise from a non-linear relationship between synaptic input and firing rate that amplifies the difference in afferent-evoked excitation between MCs and TCs. Alternatively, some other factor, such as intrinsic biophysical differences in excitability, may contribute to the differential afferent-evoked firing rates of MCs and TCs. To distinguish between these possible mechanisms, we first looked for a direct relationship between afferent-evoked firing rate and the strength of afferent-evoked excitation across MCs and TCs (Fig. 3). To discount any confounding effects of using multiple sequential stimulation pulses (e.g. failure of a synaptic response at the end of a train of stimulation pulses), we separately examined both the response to the first stimulation pulse in each stimulus train (Fig. 3*A*, *D*) and the response to the full stimulus train (Fig. 3*B*, *E*). A significant correlation existed between afferent-evoked firing rates and the rapid peak amplitude of afferent-evoked excitation (Fig. 3*B*), confirming that the strength of afferent-evoked excitation (as measured by the rapid peak current amplitude) contributes to the distinct afferent-evoked firing rates of MCs and TCs. Indeed, there was no clear difference between MC and TC afferent-evoked firing rates normalized by rapid peak current amplitudes (Fig. 3*C*). The relationship between firing rates and rapid peak current amplitudes was quite weak ($R^2 = 0.04$), however, and surprisingly no significant relationship was observed between another measure of afferent-evoked excitation strength (total charge transferred) and firing rate (Fig. 3*D*–*F*). These results thus suggest that other factors in addition to the strength of afferent-evoked excitation contribute to the difference in afferent-evoked firing rates between MCs and TCs.

We therefore next considered whether differences in overall excitability between MCs and TCs might provide a better prediction of afferent-evoked firing rate than the strength of afferent-evoked excitation. To measure excitability, we recorded the firing rates evoked by 2 s somatic step current injections ranging from 0 to 300 pA in amplitude and calculated the gains of the resulting FI curves (Fig. 3*I*). Indeed, a significant and comparatively strong relationship existed between FI curve gains and the afferent-evoked firing rates following

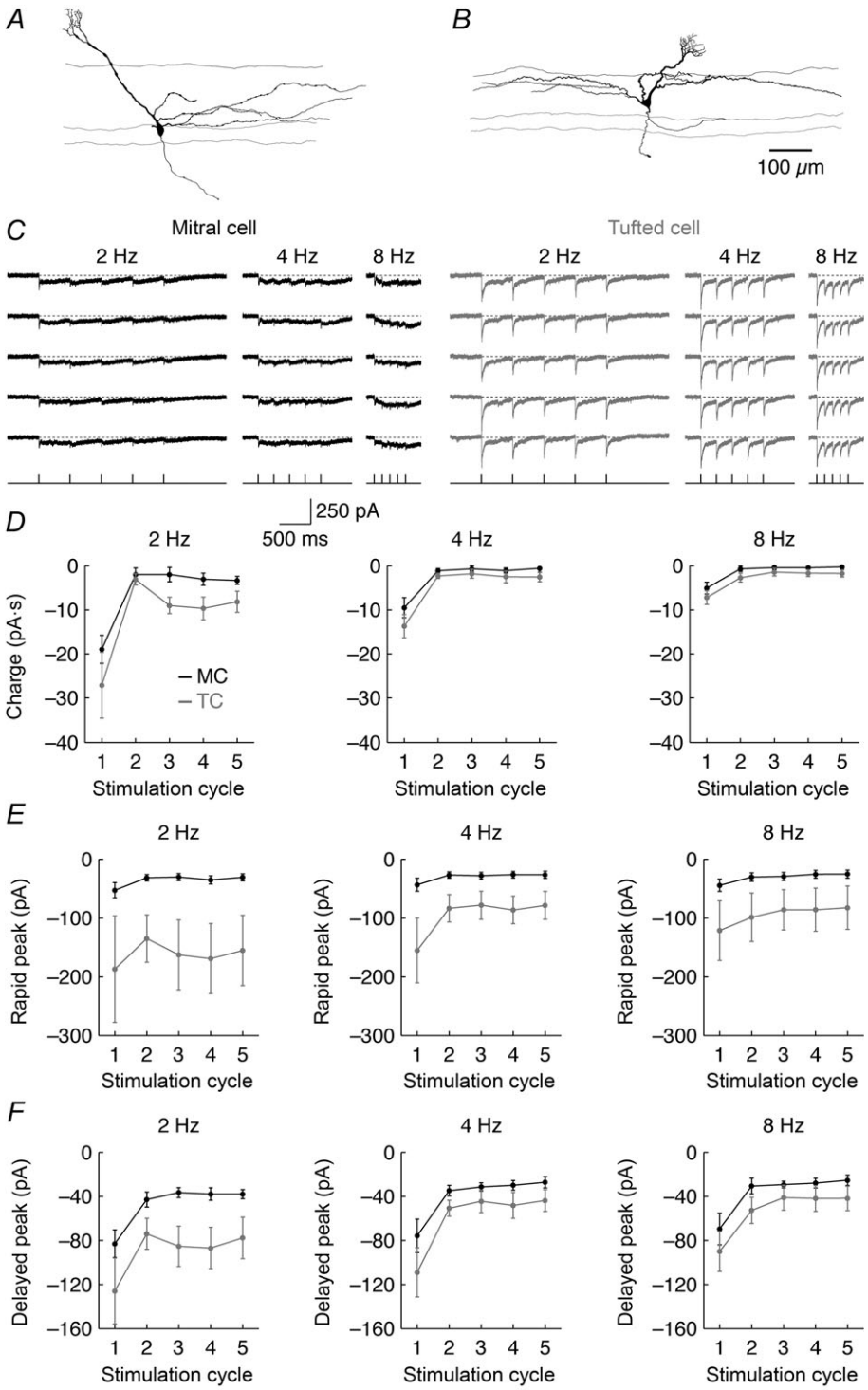

Figure 2. TCs receive greater effective afferent input than MCs
A and *B*, morphology of a representative MC (*A*) and TC (*B*). *C*, afferent-evoked synaptic input of the representative cells shown in *A* and *B* in response to 2, 4 and 8 Hz ONL stimulation. Five trials of each stimulation frequency are shown. Timing of ONL stimulation is plotted at the bottom. *D*, average charge transferred by afferent input during each stimulation cycle was significantly greater in TCs than in MCs (2 Hz: $P = 3.5 \times 10^{-3}$; 4 Hz: $P = 0.025$; 8 Hz: $P = 6.5 \times 10^{-3}$). *E*, average peak amplitude of afferent input <4 ms after ONL stimulation was significantly greater in TCs than in MCs (2 Hz: $P = 5.8 \times 10^{-5}$; 4 Hz: $P = 9.5 \times 10^{-5}$; 8 Hz: $P = 1.2 \times 10^{-3}$). *F*, average peak amplitude of afferent input >30 ms after ONL stimulation was significantly greater in TCs than in MCs (2 Hz: $P = 5.6 \times 10^{-5}$; 4 Hz: $P = 7.9 \times 10^{-3}$; 8 Hz: $P = 0.015$). Data in *D*–*F* were recorded from six MCs and seven TCs.

a single stimulation pulse (Fig. 3*G*) or a train of stimuli (Fig. 3*H*). This relationship could not be explained by any correlation between FI curve gain and the rapid peak current amplitude of afferent-evoked excitation (data not shown). Thus, these results demonstrate that differences in excitability contribute to the differences in afferent-evoked firing rates between MCs and TCs, and in turn suggest that TCs exhibit greater excitability than MCs. It is important to note, however, that these gain measurements were performed in the presence of intact synaptic transmission, and thus do not provide a pure measure of intrinsic excitability, as both MC and TC firing recruits recurrent inhibition (for review, see Schoppa & Urban, 2003). These results thus motivated a more controlled comparison of the intrinsic biophysical properties of MCs and TCs to better understand the factors contributing

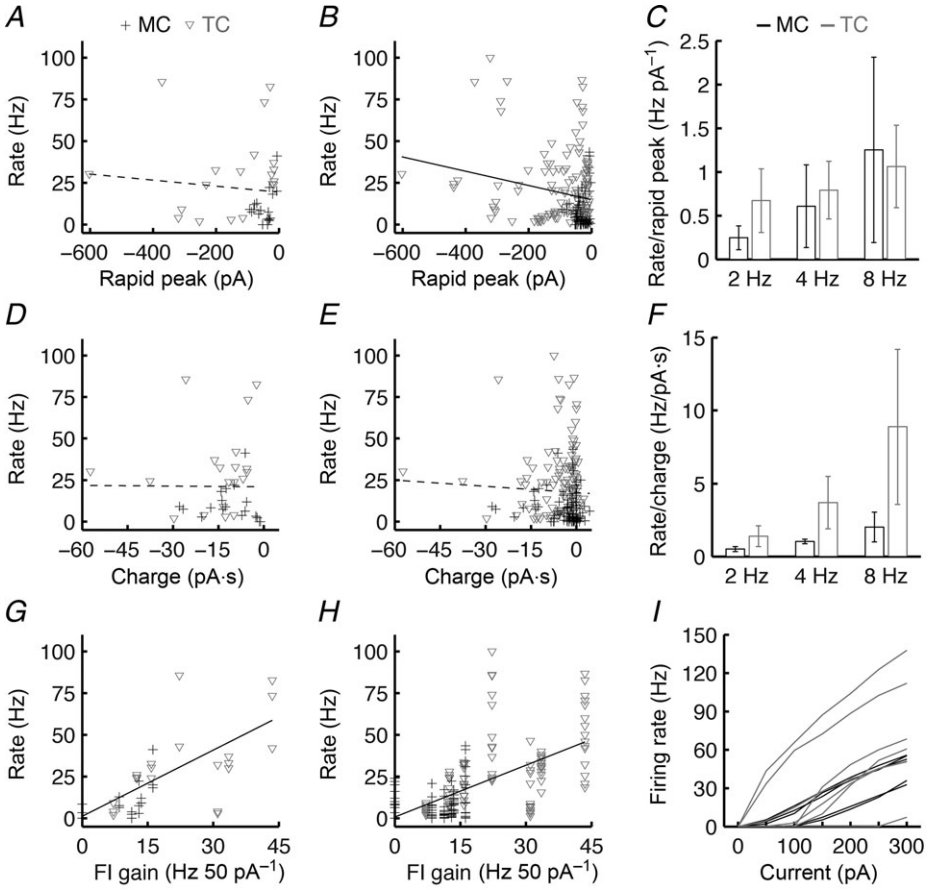

Figure 3. Differences in afferent input and excitability contribute to the higher afferent-evoked firing rates of TCs *vs*. MCs

A and *B*, average firing rates (including subthreshold trials; e.g. see Fig. 1) plotted against the average rapid peak current (e.g. see Fig. 2) evoked by ONL stimulation at 2, 4 and 8 Hz for MCs ($n = 6$) and TCs ($n = 7$). The responses to the first stimulation pulse in a train of five stimulation pulses are plotted in *A*. The responses to all stimulation pulses are plotted in *B*. Rapid peak currents weakly but significantly predicted firing rates across MCs and TCs (*B*; black line; linear regression: $P = 3.5 \times 10^{-3}$; $R^2 = 0.04$). This relationship proved insignificant when only considering the response to the first stimulation pulse in each train, however (*A*; dashed line; linear regression: $P = 0.54$). *C*, average firing rate normalized by the rapid peak current evoked by ONL stimulation at 2, 4 and 8 Hz for MCs and TCs. Error bars denote SEM. *D–F*, as in *A–C* but examining the relationship between average afferent-evoked firing rates and the total charge transferred by ONL stimulation. No significant correlation existed between rate and charge transferred in response to the first stimulation pulse (*D*; dashed line; linear regression: $P = 0.96$) or in response to the full stimulus train (*E*; dashed line; linear regression: $P = 0.52$). TCs exhibited a strong trend toward higher afferent-evoked firing rates than MCs when normalizing by the total charge transferred by afferent stimulation (*F*; $P = 0.08$, two-way ANOVA). *G* and *H*, as in *A* and *B* and *D* and *E*, but examining the relationship between average afferent-evoked firing rates and the FI curve gain measured in each MC and TC. FI curve gain significantly predicted the afferent-evoked firing rate evoked by the first ONL stimulation pulse (*G*; black line; linear regression: $P = 1.3 \times 10^{-4}$; $R^2 = 0.33$) and the entire ONL stimulation train (*H*; black line; linear regression: $P = 5.7 \times 10^{-18}$; $R^2 = 0.32$). *I*, FI curves of MCs and TCs measured from the response to somatic step current injections.

Table 1. Passive properties of MCs *vs.* TCs

	V_{rest} (mV)	R_{input} (MΩ)	τ_m (ms)	C_m (pF)	Sag amplitude (mV)
Mitral cells	-53.9 ± 4.0 ($n = 20$)	94.3 ± 40.5 ($n = 35$)	21.3 ± 9.4 ($n = 35$)	236.4 ± 94.6 ($n = 35$)	2.0 ± 2.6 ($n = 35$)
Tufted cells	-55.5 ± 4.7 ($n = 26$)	111.8 ± 51.6 ($n = 28$)	18.8 ± 8.6 ($n = 28$)	188.8 ± 110.1 ($n = 28$)	4.4 ± 6.1 ($n = 28$)
P	n.s. (0.12)	n.s. (0.23)	n.s. (0.22)	2.6×10^{-3}	n.s. (0.19)

Values are mean ± standard deviation. n.s., not significant.

to the afferent-evoked activity of MOB principal neurons.

TCs are more excitable than MCs

Currently, the intrinsic biophysical properties of MCs, but not TCs, are well characterized (cf. http://neuroelectro.org/neuron/129/ and http://neuroelectro.org/neuron/131/). Thus, to determine the contribution of intrinsic biophysical differences to the distinct afferent-evoked activity of MCs and TCs, we systematically compared the passive, action potential and spike train properties of MCs and TCs under blockade of fast synaptic transmission.

TCs demonstrated significantly lower C_m and a weak trend toward higher R_{input} than MCs (Table 1, Fig. 4*K*, *M*). These results are consistent with prior findings that TCs have smaller somata and fewer and shorter lateral dendrites than MCs (Macrides & Schneider, 1982; Orona *et al.* 1984; Igarashi *et al.* 2012; Kikuta *et al.* 2013). Reconstruction and analysis of 30 MCs and 21 TCs from our *in vitro* data set confirmed these morphological differences (Table 2; Figs S1 and S2). We additionally observed no significant difference in total process length, total process volume or convex hull volume between MC and TC apical dendritic tufts (Table 3; Figs S1 and S2), suggesting that: (1) the stronger afferent input to TCs is not due to greater overlap of TC dendrites with OSN axons within the glomerular compartment, and (2) both TC and MC apical dendritic tufts are well positioned to synaptically interact with the multitude of juxtaglomerular interneurons. Additionally, pairwise regression analysis between morphological and intrinsic biophysical properties of MCs and TCs revealed that MC R_{input} depends strongly on apical, but not lateral, dendrite volume, even though lateral dendrite volume and soma area strongly regulate MC C_m, as expected (Fig. S3). This result complements previous reports of high ion channel densities in MC apical dendrites (for review, see Migliore & Shepherd, 2002).

TCs exhibited shorter duration action potentials than MCs (Table 4, Fig. 4*E*, *H*). This difference was entirely due to a faster repolarization of TC action potentials (Table 4, Fig. 4*F*, *I*, *J*), suggesting that MCs and TCs differ in their expression of voltage-gated potassium channels. Consistent with this hypothesis, TCs exhibited significantly faster AHP kinetics than MCs, and further tended to exhibit larger AHP amplitudes and a slower action potential rising phase than MCs (Table 4, Fig. 4*F*, *G*, *I*, *J*).

Both classes of MOB principal neurons exhibited considerable heterogeneity in their rheobase current (Table 5), consistent with previous investigation of MC rheobase values (Angelo & Margrie, 2011). The lack of significant difference between MC and TC rheobase values (Table 5) thus suggests that the substantially higher fraction of subthreshold responses to afferent-evoked input recorded in MCs relative to TCs (Fig. 1) is principally due to differences in the strength of afferent-evoked excitation between MCs and TCs. We likewise found no significant difference between, and a substantial degree of heterogeneity in, MC and TC first-spike latencies at rheobase (Table 5). This observation is consistent with the strong dependence of odour-evoked MC and TC latency differences on extrinsic, synaptic properties (Fukunaga *et al.* 2012).

The two classes of MOB principal neurons exhibited markedly different levels of excitability in response to somatic step current injections (Table 5, Fig. 5), confirming our earlier results (Fig. 3). Both the average FI curve gain and the peak instantaneous firing rate of TCs doubled those of MCs (Table 5, Fig. 5*C*–*E*). These differences probably arise, in part, from the narrower action potentials and the faster AHP kinetics in TCs, which enable TC membrane potentials to more quickly 'reset' following an action potential than MC membrane potentials. The weak trend toward higher R_{input} in TCs may also partially contribute to the greater excitability of TCs *vs.* MCs. We note, however, that there are numerous examples in our dataset where TCs exhibit greater excitability than MCs despite equal or lower R_{input} (Fig. 5*F*).

In total, we thus find that in addition to extrinsic synaptic differences, the two classes of MOB principal neurons exhibit significant differences in intrinsic biophysical properties. In particular, TCs are intrinsically twice as excitable as MCs on average, and this greater excitability contributes significantly to the higher

afferent-evoked firing rates observed in TCs. Moreover, differences in action potential waveforms probably influence synaptic propagation of MC *vs.* TC activity to MOB interneurons and downstream cortical targets (see Discussion).

TCs stutter more than MCs

Our results thus far have focused on the strength of afferent-evoked activity in MOB principal neurons. However, several studies have demonstrated that the odour-specific *temporal patterning* of action potentials also critically contributes to the encoding of olfactory information (for review, see Friedrich, 2006; Bathellier *et al.* 2010). Indeed, Haddad *et al.* (2013) recently confirmed that olfactory cortex can decode differences in spike timing of MOB principal neurons. We thus next examined how MCs and TCs transform input into specific temporal patterns of action potentials.

Principal neurons of the MOB exhibit diverse firing modes *in vivo*, transforming afferent input into both regular and irregular patterns of action potentials

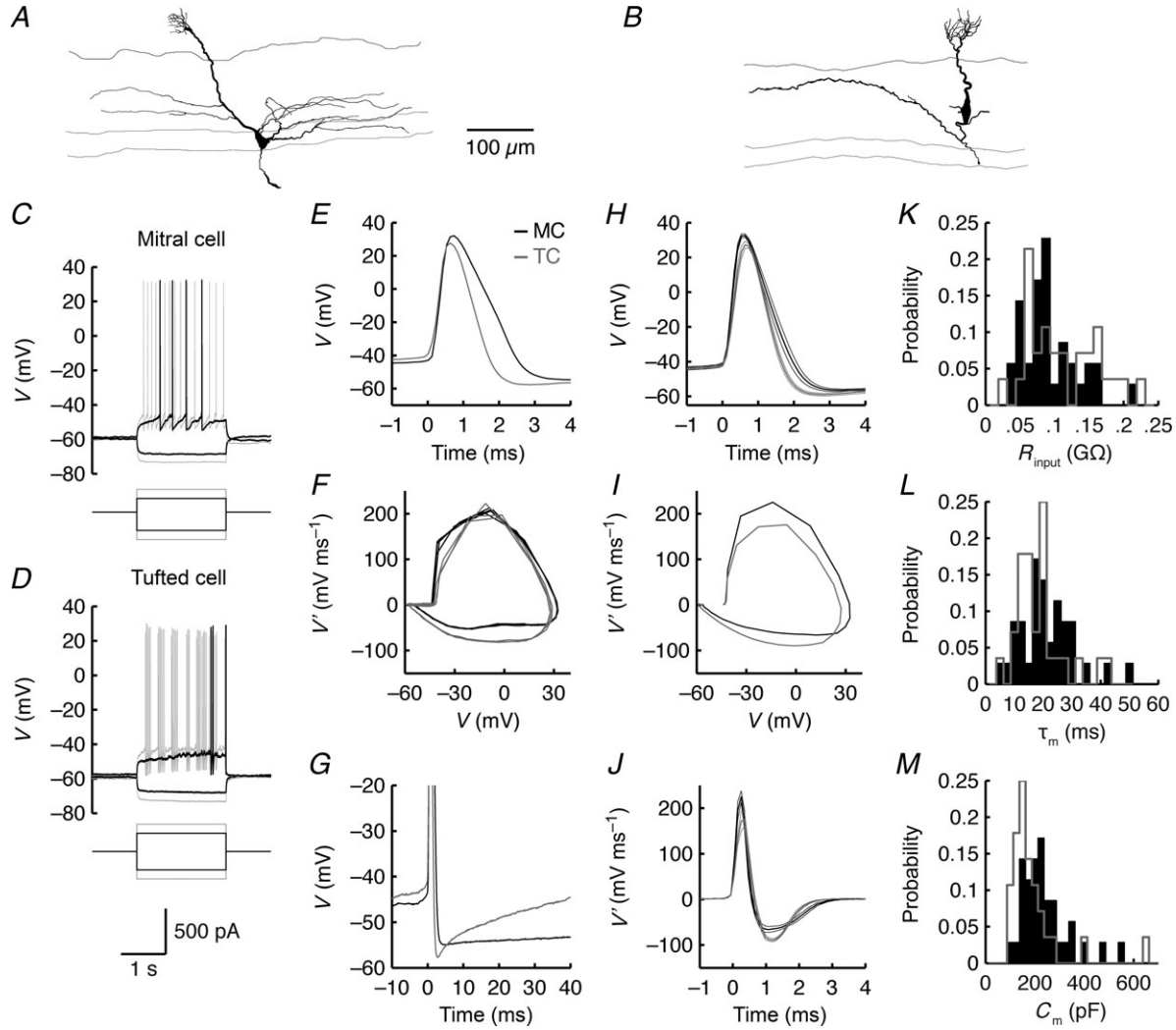

Figure 4. TCs exhibit faster action potential and AHP kinetics than MCs
A–D, morphology (*A*, *B*) and voltage responses (*C*, *D*) of a representative MC (*A*, *C*) and TC (*B*, *D*) to step current injections. *E*, waveform of the first action potentials evoked by the weakest suprathreshold input (black suprathreshold traces in *C* and *D*). *F*, phase plot of membrane potentials during the weakest suprathreshold input. *G*, AHPs following the action potentials plotted in *E*. *H*, average action potential waveform. Thin lines denote mean ± SEM. *I*, phase plot of average action potential derivative *vs*. average action potential waveform across MC and TC populations. *J*, average temporal evolution of membrane potential derivatives during the first action potential evoked by the weakest suprathreshold input. Averages taken over 10 MCs and 12 TCs in *H–J*. *K–M*, distributions of R_{input} (*K*), τ_m (*L*) and C_m (*M*) calculated from hyperpolarizing step current injections (e.g. as plotted in *C* and *D*) over 35 MCs and 28 TCs.

Table 2. Somatodendritic morphological properties of MCs *vs.* TCs

		Lateral dendrites		Apical dendrites	
	Soma area (μm^2)	Σ Length (μm)	Σ Volume (μm^3)	Σ Length (μm)	Σ Volume (μm^3)
Mitral cells	349.0 ± 106.4 ($n = 30$)	2766.0 ± 1792.2 ($n = 30$)	3433.8 ± 2221.7 ($n = 30$)	258.3 ± 60.6 ($n = 30$)	3025.0 ± 1588.3 ($n = 30$)
Tufted cells	236.2 ± 93.1 ($n = 21$)	1624.8 ± 642.6 ($n = 21$)	1937.4 ± 838.8 ($n = 21$)	144.4 ± 44.3 ($n = 21$)	1235.0 ± 627.0 ($n = 21$)
P	2.3×10^{-4}	3.5×10^{-3}	0.01	7.1×10^{-8}	7.9×10^{-6}

Values are mean ± standard deviation.

Table 3. Tuft morphological properties of MCs *vs.* TCs

	Σ Length (μm)	Σ Volume (μm^3)	Convex hull (μm^3)
Mitral cells	967.6 ± 464.2 ($n = 30$)	816.9 ± 479.7 ($n = 30$)	49,040.8 ± 34,375.5 ($n = 30$)
Tufted cells	838.7 ± 356.7 ($n = 21$)	599.2 ± 411.4 ($n = 21$)	38,601.4 ± 21,749.2 ($n = 21$)
P	n.s. (0.56)	n.s. (0.08)	n.s. (0.37)

Values are mean ± standard deviation. n.s., not significant.

(Buonviso *et al.* 2003; Margrie & Schaefer, 2003; Schaefer *et al.* 2006; Bathellier *et al.* 2008; Cury & Uchida, 2010; Carey & Wachowiak, 2011; Shusterman *et al.* 2011). We and others have recently demonstrated that at least a portion of this temporal patterning of MOB activity arises from the intrinsic ability of MCs to exhibit both tonic and stuttering firing modes (Padmanabhan & Urban 2010; Angelo & Margrie, 2011; Fadool *et al.* 2011; Tucker *et al.* 2013). To investigate whether TCs exhibit similar firing mode diversity, we compared the regularity of MC and TC spike trains evoked by somatic step current injections (Table 5, Fig. 6). Similar to MCs, TCs exhibited diverse firing modes (Fig. 6*A*, *B*), with output ranging from tonic firing with varying degrees of spike frequency adaptation and narrow ISI distributions to irregular stuttering with highly skewed ISI distributions (Fig. 6*C*, *D*) highly reminiscent of some populations of cortical and subcortical fast-spiking interneurons (for review, see Markram *et al.* 2004; Tepper & Bolam, 2004). Furthermore, TCs on average fired more irregularly than MCs, as measured by the CV_{ISI} (Table 5, Fig. 6*E*–*H*). This difference in regularity was not just due to differences in firing rate, as TCs likewise exhibited significantly higher CV_{ISI} than MCs when we controlled for rate (Table 5). Moreover, CV_{ISI} and excitability (as measured by FI curve gain) were not well correlated (Fig. 6*I*). These results are also consistent with a recent characterization of the firing patterns of MCs and TCs *in vitro* in response

Table 4. Action potential properties of MCs *vs.* TCs

	$V_{threshold}$ (mV)	Amplitude (mV)	FWHM (ms)	Rising slope (mV ms^{-1})	Falling slope (mV ms^{-1})	AHP (mV)	$T_{AHP\ 50\%}$ (ms)
Mitral cells	−42.2 ± 3.0 ($n = 10$)	76.2 ± 5.4 ($n = 10$)	1.06 ± 0.20 ($n = 10$)	237.9 ± 48.4 ($n = 10$)	−72.2 ± 20.4 ($n = 10$)	14.8 ± 3.2 ($n = 10$)	58.2 ± 77.5 ($n = 35$)
Tufted cells	−42.5 ± 2.9 ($n = 12$)	72.1 ± 5.5 ($n = 12$)	0.87 ± 0.10 ($n = 12$)	197.9 ± 62.5 ($n = 12$)	−91.4 ± 13.0 ($n = 12$)	16.8 ± 3.3 ($n = 12$)	20.5 ± 20.1 ($n = 28$)
P-value	n.s. (0.82)	n.s. (0.11)	0.03	n.s. (0.05)	0.03	n.s. (0.08)	5.8×10^{-3}

Values are mean ± standard deviation. n.s., not significant.

Table 5. Spike train properties of MCs *vs.* TCs

	Rheobase (pA)	Rheobase spike latency (ms)	Peak instantaneous rate (Hz)	FI curve gain (Hz 50 pA^{-1})	$CV_{ISI,\ \sim 20\ Hz}$
Mitral cells	111.4 ± 55.7 ($n = 35$)	510.0 ± 486.0 ($n = 35$)	62.8 ± 15.9 ($n = 35$)	9.8 ± 3.8 ($n = 35$)	0.45 ± 0.29 ($n = 35$)
Tufted cells	94.6 ± 49.7 ($n = 28$)	402.3 ± 479.5 ($n = 28$)	120.1 ± 28.4 ($n = 28$)	20.3 ± 7.2 ($n = 28$)	0.80 ± 0.43 ($n = 28$)
P	n.s. (0.22)	n.s. (0.26)	9.5×10^{-11}	1.5×10^{-8}	3.3×10^{-4}

Values are mean ± standard deviation. n.s., not significant.

to spontaneous LLDs (Ma & Lowe, 2010). Indeed, we were able to confirm that the firing mode measured by somatic step current injection closely corresponds to the firing mode evoked by afferent input (Fig. S4). Thus, we expect that TCs exhibit diverse firing modes and fire more irregularly than MCs *in vivo*.

Interestingly, MCs exhibited a significant age-dependent decrease in firing regularity, particularly after 18 days of age (Fig. S5). Thus, different developmental time courses may partially explain the more irregular firing of TCs than MCs in our dataset. We note, however, that even mature MCs exhibit clear differences in their stuttering firing patterns compared to TCs (see below).

Visual inspection of spiking patterns further suggested that the way in which irregularly firing MCs and TCs stutter is different. Specifically, TCs fired clusters of high-frequency action potentials separated by long ISIs between clusters (Fig. 6*B*). In contrast, MCs exhibited comparatively similar within-cluster and between-cluster ISIs (Fig. 6*A*). In other words, the instantaneous firing rate of TCs departed substantially from the mean rate for each spike train, while the instantaneous firing rate of MCs more closely tracked the mean rate. To quantify

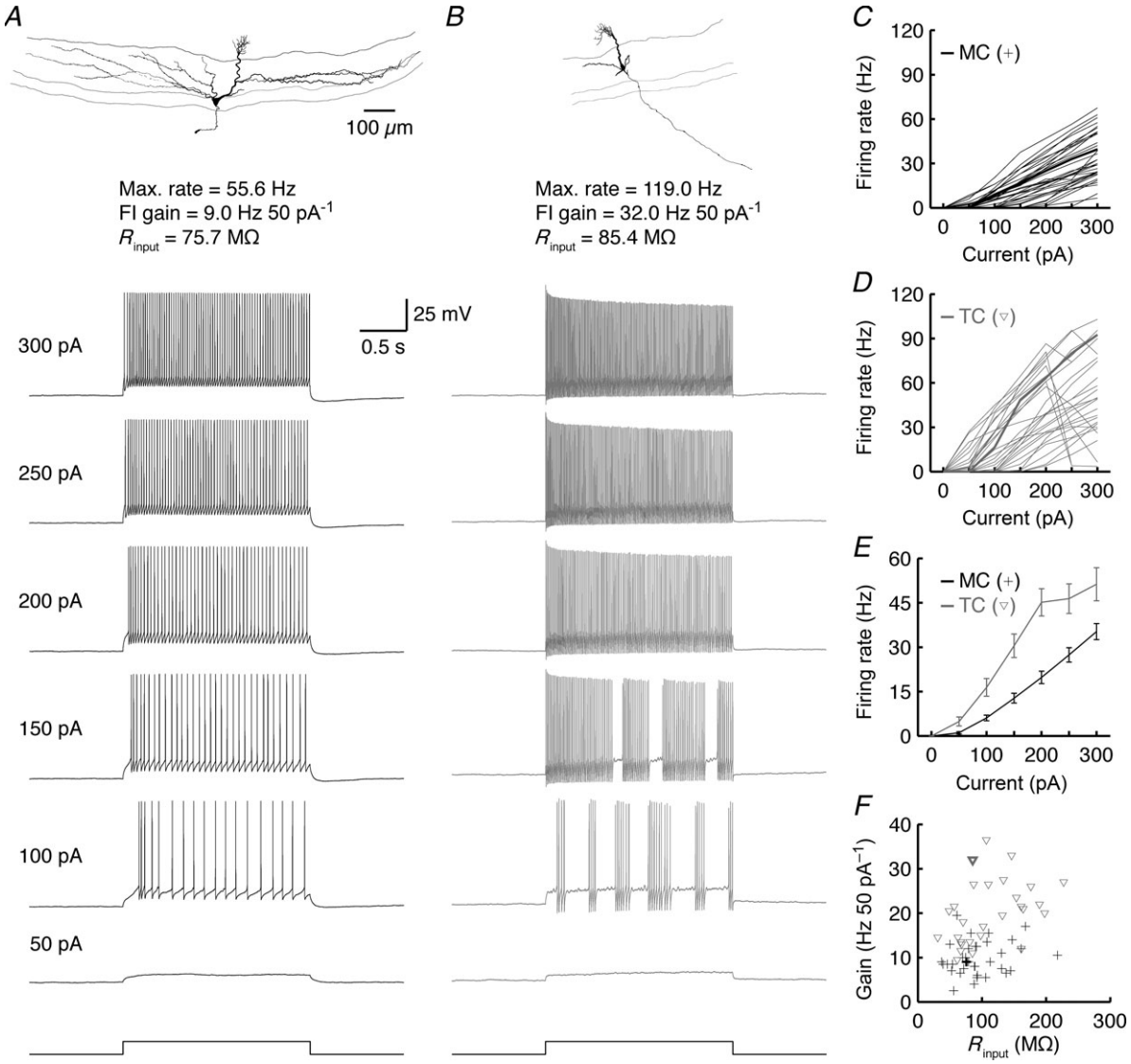

Figure 5. TCs are intrinsically more excitable than MCs
A and *B*, morphology and firing response to various step current injections of a representative MC (*A*) and TC (*B*). *C* and *D*, FI relationships for 35 MCs (*C*) and 28 TCs (*D*). Thick lines correspond to representative cells shown in *A* and *B*. Note that several TCs go into depolarization block at high step current amplitudes. *E*, average FI relationships across all MCs and TCs. Error bars denote SEM. *F*, FI curve gain *vs*. R_{input} across MCs and TCs. Thick-lined symbols correspond to representative cells.

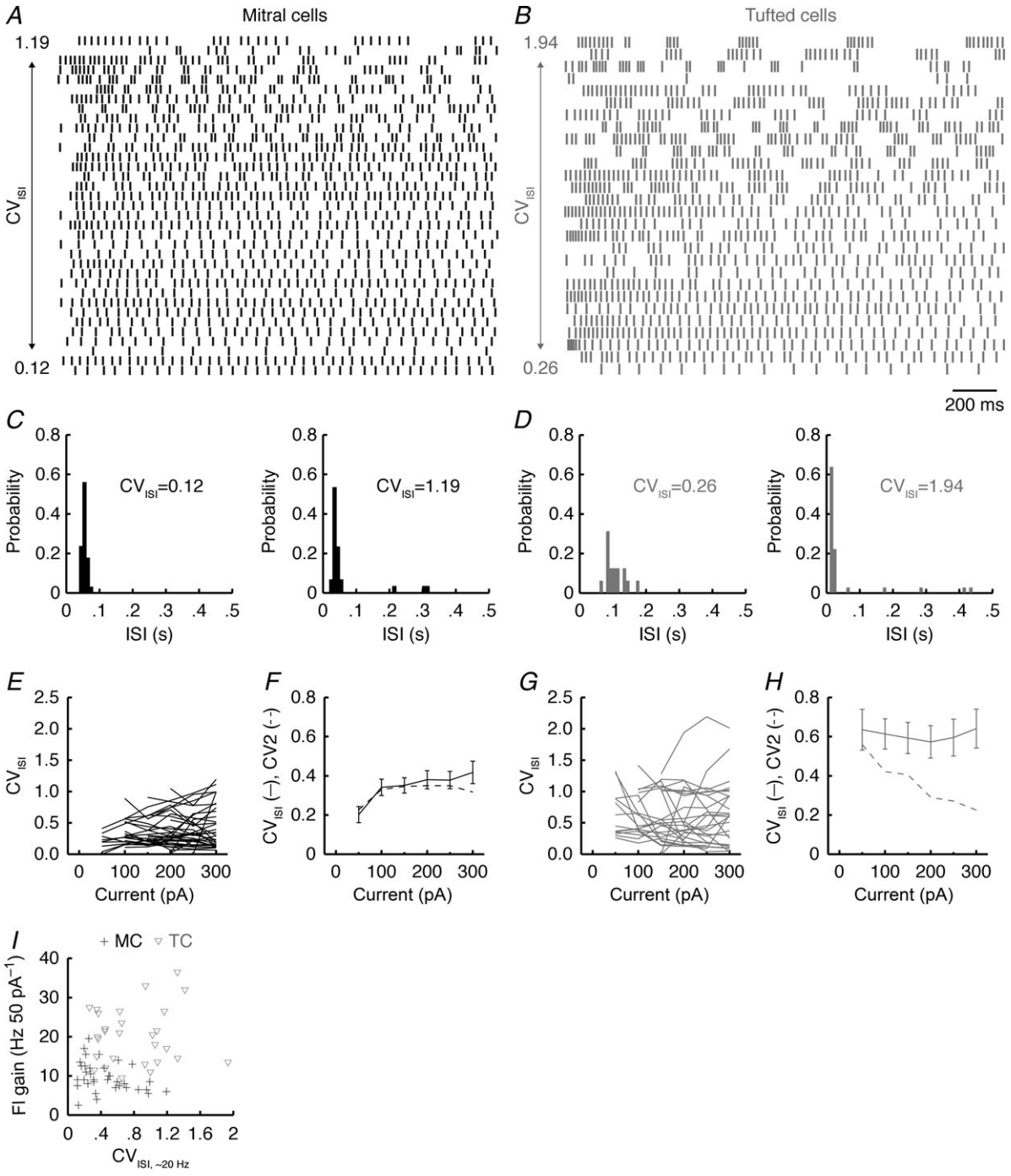

Figure 6. TCs exhibit diverse firing modes and more irregular firing than MCs
A and *B*, spike raster plots across 35 MCs (*A*) and 28 TCs (*B*) for firing responses to 2 s step current injections coming closest to 20 Hz. Spike trains are ordered according to CV_{ISI}, with minimum and maximum CV_{ISI} values shown. *C* and *D*, ISI distributions of the most regular and irregular MC (*C*) and TC (*D*) spike trains shown in *A* and *B*. *E*, CV_{ISI} across multiple step current injection amplitudes for MCs. *F*, average CV_{ISI} across all MCs for multiple step current injection amplitudes. Error bars denote SEM. *G* and *H*, as in *E* and *F* for TCs. Note that TCs demonstrated a significantly higher CV_{ISI} than MCs (compare *F* and *H*; $P = 5.8 \times 10^{-9}$, two-way ANOVA with *post hoc* Tukey's test). Note also the close correspondence between the average CV_{ISI} and CV2 for MCs (*F*) but not for TCs (H). *I*, FI curve gain *vs*. CV_{ISI} across MCs and TCs.

this effect, we calculated the instantaneous ISI variability normalized to the instantaneous ISI and averaged this across the spike train to yield a single value per spike train. This metric, called 'CV2' (Holt *et al.* 1996), is equivalent to CV_{ISI} for a regular spike train and for a perfectly random spike train (i.e. a homogeneous Poisson process) but is lower than CV_{ISI} for a slowly rate-modulated spike train (e.g. a spike train with highly discrete bursts). Confirming our initial observations, MCs exhibited nearly identical CV_{ISI} and CV2 (Fig. 6*F*). In contrast, TCs exhibited a markedly higher CV_{ISI} than CV2 (Fig. 6*H*), especially at higher input strengths. Thus, the greater overall firing irregularity of TCs compared to MCs arises from a greater propensity of TCs to fire highly discrete clusters of action potentials.

Membrane potential sag predicts stuttering in both TCs and MCs

The differences in MC *vs.* TC firing regularity suggest that distinct ionic mechanisms may regulate MC *vs.* TC firing modes. Toward this end, Angelo & Margrie (2011) recently demonstrated that differential expression of hyperpolarization-activated cation channels across MCs is related to MC firing regularity. In their study, MCs exhibiting more sag in response to a hyperpolarizing step current (i.e. larger positive sag amplitude) tended to fire more regularly than MCs exhibiting less sag. We therefore next examined the distribution of sag responses in MCs and TCs to determine if: (1) a similar relationship exists between TC firing regularity and sag, and (2) if the greater propensity of TCs to stutter is predicted by the distribution of TC sag amplitudes.

In agreement with Angelo and Margrie (2011), we observed a broad diversity of sag responses in MCs (Fig. 7*E*), including both negative (Fig. 7*A*) and positive (Fig. 7*B*) sag amplitudes. TCs likewise exhibited a broad distribution of sag responses (Table 1, Fig. 7*C–E*). Interestingly, sag amplitudes strongly predicted rheobase values in both classes of MOB principal neurons (Fig. 7*G*), as previously reported for MCs (Angelo & Margrie, 2011). To statistically test for a relationship between sag amplitude and firing mode, we performed linear regression between sag amplitude and the CV_{ISI} measured at a mean rate of ∼20 Hz. MCs demonstrated a significant negative relationship between sag amplitude and CV_{ISI} (Fig. 7*F*), strengthening the findings of Angelo and Margrie (2011). In turn, TCs demonstrated an even stronger relationship between sag amplitude and CV_{ISI} (Fig. 7*F*). Thus, sag amplitude is broadly distributed across both classes of MOB principal neurons and is predictive of firing mode. We note, however, that the greater propensity of TCs than MCs to stutter is not predicted by sag, as MC and TC sag amplitudes did not significantly differ on average (Table 1, Fig. 7*E*). Thus, our results support the hypothesis that distinct ionic mechanisms regulate MC *vs.* TC firing modes.

Discussion

For more than a century, principal neurons of the MOB have been divided between MCs and TCs on the basis of morphological and laminar differences (Cajal, 1911). Here, we report the first systematic comparison of MC and TC intrinsic biophysical properties, and we identify several key functional features by which these two cell classes differ. Foremost, TCs are more excitable than MCs. This difference in excitability emerges, at least partially, from narrower action potentials and faster AHP kinetics in TCs, engendering shorter refractory periods in TCs than in MCs. The greater excitability of TCs, combined with stronger afferent-evoked excitation, helps drive the stronger afferent-evoked firing responses in TCs compared to MCs. Additionally, while both MCs and TCs exhibit diverse firing modes, TCs demonstrate a greater propensity to 'stutter', i.e. to fire discrete clusters of high frequency action potentials separated by long pauses. Hyperpolarization-activated currents predict firing regularity in both MCs and TCs, but cannot directly explain the greater firing irregularity of TCs. In total, these results reveal multiple mechanisms through which the two classes of MOB principal neurons can transform convergent sensory input into complementary olfactory information.

Physiological role of differences in afferent-evoked activity between MCs and TCs

TCs exhibit greater excitability and stronger afferent-evoked excitation than MCs. The combination of these properties may contribute to at least three physiological roles in olfactory processing: (1) differential encoding of complementary sensory information, (2) differential regulation of sensory processing by changes in network states and (3) collective encoding of sensory intensity (i.e. odour concentration).

First, the combination of greater excitability and stronger afferent-evoked excitation reliably drives short latency, high rate TC firing (Fig. 1), yielding a high fidelity afferent-evoked signal. In contrast, the lower excitability and weaker afferent-evoked excitation of MCs, combined with more extensive lateral inhibition (Ezeh *et al.* 1993; Christie *et al.* 2001; Phillips *et al.* 2012) and potentially stronger afferent-evoked inhibition (see below), yields lower firing rates and more variable firing latencies (Fig. 1), attributes which foster diverse temporal patterning of odour-evoked principal neuron firing (Bathellier *et al.* 2008; Cury & Uchida, 2010; Shusterman *et al.* 2011; Kato *et al.* 2012). Moreover, the weaker afferent-evoked excitation and stronger inhibition of MCs additionally supports broader inhibitory molecular receptive ranges

(MRRs) in MCs than in TCs (Nagayama *et al.* 2004; Kikuta *et al.* 2013). In total, these observations broadly support an emerging view (e.g. see Nagayama *et al.* 2010; Schaefer & Margrie, 2012; Igarashi *et al.* 2012; Fukunaga *et al.* 2012) that TCs may employ a robust labelled-line code of first-order sensory information (e.g. odour identity) while MCs employ a more flexible population-wide temporal code of second-order sensory information (e.g. odour context and valence). Of note, this hypothesis is in direct accordance with the extensive axonal projections of MCs to piriform, entorhinal and amygdaloid regions and the limited axonal projections of TCs to anterior piriform regions (Nagayama *et al.* 2010; Igarashi *et al.* 2012).

Second, differences in intrinsic excitability and afferent-evoked excitation probably also yield distinct susceptibilities of MCs and TCs to changes in network state. In particular, recent evidence shows that enhanced cholinergic signalling in the glomerular microcircuit, such as during elevated attentiveness, sharpens the odour tuning of MCs (Ma & Luo, 2012). Mechanistically, cholinergic modulation of MC tuning depends on the ability of augmented afferent-evoked inhibition to

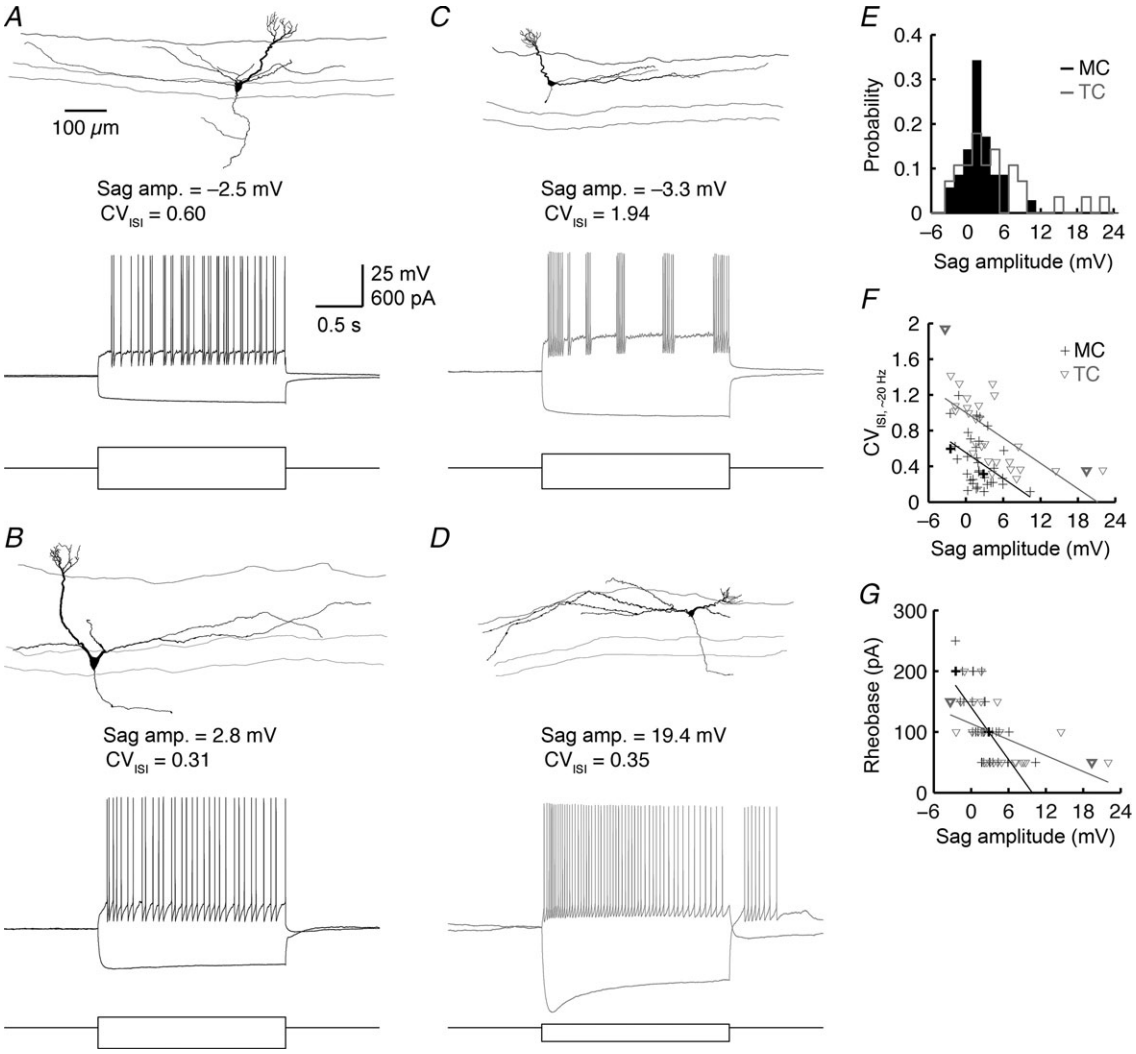

Figure 7. Sag amplitude predicts MC and TC firing mode
A, morphology and membrane potential sag and spiking responses of a representative MC with negative sag amplitude. Spiking response shows the evoked response closest to 20 Hz, where CV_{ISI} is measured. *B*, as in *A*, but for a MC with positive sag amplitude. *C* and *D*, as in *A* and *B*, but for two representative TCs. Note that the slow recovery from the large sag amplitude in *D* is sufficient to evoke several rebound action potentials. *E*, distribution of sag amplitudes for 35 MCs and 28 TCs. *F*, CV_{ISI} *vs*. sag amplitude. MC sag amplitude significantly predicts CV_{ISI} (black line; linear regression: $P = 9.4 \times 10^{-3}$; $R^2 = 0.19$). TC sag amplitude likewise predicts CV_{ISI} (grey line; linear regression: $P = 7.3 \times 10^{-5}$; $R^2 = 0.46$). Thick-lined symbols correspond to representative cells in *A*–*D*. *G*, rheobase *vs*. sag amplitude. Sag amplitude significantly predicts rheobase in both MCs (black line; linear regression: $P = 9.4 \times 10^{-6}$; $R^2 = 0.45$) and TCs (grey line; linear regression: $P = 3.2 \times 10^{-3}$; $R^2 = 0.29$).

block weak afferent-evoked activity in MCs (D'Souza & Vijayaraghavan, 2012; D'Souza *et al.* 2013). Our current results thus suggest that TCs, which demonstrate stronger afferent-evoked excitation and greater excitability than MCs, should be less susceptible to effects of cholinergic modulation than MCs. Of note, this hypothesis may be directly examined through re-analysis of several recent datasets of MOB principal neuron activity collected across different brain states (Kato *et al.* 2012; Blauvelt *et al.* 2013; Wachowiak *et al.* 2013).

Finally, the interaction of afferent-evoked *inhibition* and differences in intrinsic excitability between homotypic MCs and TCs (i.e. MCs and TCs with apical dendritic tufts in the same glomerulus) may be critical to the encoding of stimulus intensity during sparse glomerular activation (Smear *et al.* 2013). Three arguments support this possibility. (1) MC activity is more strongly influenced by afferent-evoked inhibition than TC activity. MC firing is strongly regulated by afferent-evoked inhibition (Shao *et al.* 2012), and this inhibition is stable over sequential afferent stimulation cycles (Shao *et al.* 2013), in contrast to the depressing afferent-evoked excitation that we observe (Fig. 2*D*; but see Cang & Isaacson, 2003). The shifting balance of inhibition and excitation probably contributes to adaptation of MC firing rates with repeated afferent stimulation (Fig. 1*E*). In contrast, the stable suprathreshold response of TCs to sequential afferent stimulation cycles (Fig. 1*E*) suggests that TCs are less influenced by afferent-evoked inhibition than MCs. Indeed, Fukunaga *et al.* (2012) have compellingly shown that inhibition (probably mediated by PGCs) strongly modulates the latency of odour-evoked firing in MCs but not in TCs. The greater influence of afferent-evoked inhibition on MC activity could arise from greater PGC–MC connectivity or from the greater excitability of TCs rendering such inhibition less effective. (2) The strength of afferent-evoked inhibition directly regulates the odour concentration dependence of MOB principal neuron activity. In their study, Fukunaga *et al.* (2012) additionally demonstrated that increasing odour concentration reduces MC, but not TC, firing latencies, paralleling the effect of blocking inhibition. Moreover, the preferential regulation of MC activity by afferent-evoked inhibition and a direct link between such inhibition and concentration dependence may explain the lower odour concentration threshold and greater odour concentration invariance of TC *vs.* MC activity (Fukunaga *et al.* 2012; Igarashi *et al.* 2012; Kikuta *et al.* 2013). (3) Short latency high rate TC firing significantly recruits inhibition onto MCs. Increasing odour concentrations reduces MC firing latencies by increasing excitatory input while afferent-evoked inhibition remains constant (Margrie *et al.* 2001; Cang & Isaacson, 2003). This suggests that at least two pathways mediate odour-evoked excitation and inhibition onto MCs. Both OSNs and ETCs are probably important sources of odour concentration-dependent MC excitation (De Saint Jan *et al.* 2009; Gire & Schoppa, 2009; Najac *et al.* 2011; Gire *et al.* 2012). In turn, TCs, which exhibit odour concentration-invariant activity, are probably the primary source driving odour concentration-independent, PGC-mediated inhibition onto MCs. Consistent with this hypothesis, Livneh *et al.* (2014) have shown that the phase of spontaneous and odour-evoked PGC firing *in vivo* closely matches the phase of spontaneous and odour-evoked TC, but not MC, firing *in vivo* (Fukunaga *et al.* 2012). While TCs can also directly excite MCs (Najac *et al.* 2011), such lateral excitation between homotypic MOB principal neurons is heavily counterbalanced by inhibition (Urban & Sakmann, 2002) and may serve primarily to regulate spike-time synchrony (Schoppa & Westbrook, 2002). In total, changes in odour concentration thus lead to decodable differences in firing latencies between homotypic MCs and TCs through the interaction of afferent-evoked inhibition and greater TC *vs.* MC excitability and afferent-evoked excitation.

While speculative, the proposed mechanism for encoding odour concentration within a single glomerulus can explain recent *in vivo* findings (Smear *et al.* 2013) and motivates multiple new experiments that will be critical to our understanding of olfactory processing. Foremost among these experiments is the careful dissection of inhibitory interactions between homotypic MCs and TCs. To our knowledge, the ability of MCs and TCs to directly inhibit each other by recruiting PGCs has been widely assumed but remains to be directly demonstrated. It is also possible that the proposed afferent-evoked TC-to-MC inhibition could involve granule cells (GCs) and/or EPL interneurons (Huang *et al.* 2013; Kato *et al.* 2013; Miyamichi *et al.* 2013), cells classically viewed to mediate 'lateral inhibition' between MCs and TCs. These alternative circuit pathways are less likely to mediate the described afferent-evoked inhibition, however, given the more variable and longer latency recruitment of GCs *vs.* PGCs (Shao *et al.* 2012) and the tremendous numerical superiority of PGCs to EPL interneurons (Parrish-Aungst *et al.* 2007), but nevertheless require investigation. Also important will be the direct evaluation of afferent-evoked inhibition onto TCs. Finally, a causal link between TC activity and afferent-evoked inhibition onto MCs predicts a negative correlation between excitatory and inhibitory MRRs of homotypic TC and MCs, respectively – an intriguing hypothesis testable through re-analysis of recent published data (Kikuta *et al.* 2013).

Physiological role of differences in firing regularity between MCs and TCs

The expression of highly regular, tonic firing *vs.* irregular firing of discrete action potential clusters will significantly impact at least three components of neural signalling in

olfaction. First, the ability of slowly modulated inputs (e.g. sniff-coupled afferent input) to phase-lock spike timing (Schaefer *et al.* 2006) is greater in stuttering *vs.* regular firing MOB principal neurons (Balu *et al.* 2004). The higher prevalence of stuttering in TCs that we observed thus suggests that TCs may generate a reliable afferent-evoked signal across consecutive sniffs, while MC spike timing evolves (Patterson *et al.* 2013). The higher prevalence of stuttering in TCs may also help to explain the greater locking of TC *vs.* MC firing to respiration *in vivo* (Phillips *et al.* 2012). Second, we have recently demonstrated that the temporal patterning of MOB principal neuron input to anterior piriform cortex directly controls the propagation of activity between the MOB and cortex (Oswald & Urban, 2012*b*). This result, together with our current findings of differences in firing regularity between MCs and TCs, suggests that TCs propagate olfactory information to anterior piriform cortex differently than MCs do. Third, and relatedly, tonic *vs.* stuttering firing modes probably differentially recruit MOB interneurons, such as GCs, EPL interneurons and PGCs. The impact of firing mode on GC recruitment may further lead to differential recruitment of activity-dependent lateral inhibition (Arevian *et al.* 2008) between stuttering *vs.* regularly firing pairs of MOB principal neurons. Significant differences in action potential waveforms between MCs and TCs also may abet differences in interneuron recruitment via differential activation of voltage-gated calcium channels at release sites (e.g. see King & Meriney, 2005).

Ionic and dynamic mechanisms of firing mode diversity in MOB principal neurons

Defining the mechanisms driving stuttering will be a critical step in understanding the physiological roles of firing mode diversity in MCs and TCs. In both theoretical and experimental studies, neuronal stuttering is often attributed to the interaction of fast spiking dynamics with a slower, perithreshold-activated outward current, in which outward conductance incrementally accumulates with each action potential until firing is temporarily blocked, yielding overall firing dynamics known as elliptic bursting (e.g. see Rinzel & Ermentrout, 1989; Rush & Rinzel, 1995; Balu *et al.* 2004; Golomb *et al.* 2007). This mechanism has specifically been suggested to explain stuttering in MCs through the cumulative de-inactivation of D-type potassium channels (probably representing channels consisting of Kv1.x subunits) across a cluster of action potentials (Balu *et al.* 2004). In contrast to this deterministic mechanism, stuttering can also occur stochastically (with an arbitrary number of action potentials per cluster) given subthreshold oscillations and a perithreshold-activated outward current with sufficiently fast activation kinetics (Golomb *et al.* 2007; Stiefel *et al.* 2013). While both of these mechanisms are thus consistent with the activity patterns we have recorded in MCs and TCs, their functional consequences on stuttering regularity are significantly different (S. D. Burton *et al.* unpublished observations), motivating further investigation. Of interest, TCs demonstrated a greater propensity to stutter and faster AHP kinetics than MCs, suggesting that TC stuttering may be more dominated by stochastic dynamics than MC stuttering.

Our results additionally corroborate the relationship between membrane potential sag amplitude and MC firing regularity first identified by Angelo & Margrie (2011), and further extend this relationship to TCs. While the correlation between sag and MOB principal neuron firing mode thus seems robust, it is not obvious how a hyperpolarization-activated current can modulate suprathreshold activity. Critically, both hyperpolarization-activated cation channels and perithreshold-activated Kv1.3 channels are differentially expressed across MCs in an activity- and experience-dependent manner (Fadool *et al.* 2000, 2011; Tucker and Fadool, 2002; Angelo *et al.* 2012; Tucker *et al.* 2013), further arguing that broad biophysical diversity across principal neurons is a programmed coding feature of the MOB (Padmanabhan & Urban 2010; Tripathy *et al.* 2013). Full understanding of the mechanisms driving stuttering will ultimately require a complete developmental characterization of firing modes across neonatal to adult MCs and TCs.

Functional classification of TCs into a single cell class distinct from MCs and ETCs

Cajal originally divided TCs into internal/deep, middle and external/superficial TCs on the basis of laminar depth (for a review, see Macrides *et al.* 1985). Here, we have restricted our classification of TCs into a single cell class based on four recent lines of evidence arguing that TCs positioned throughout the EPL are more similar to each other than to MCs and ETCs. (1) All TCs exhibit similar intra- and extra-bulbar axonal projections that are distinct from MC projections (Ghosh *et al.* 2011; Igarashi *et al.* 2012). (2) All TCs exhibit similar phase locking to the respiratory cycle that is distinct from the phase of the respiratory cycle that MCs lock to (Fukunaga *et al.* 2012). (3) All TCs exhibit a stronger monosynaptic OSN input than MCs (Fig. 2; Gire *et al.* 2012). (4) Unbiased principal components analyses of morphological and functional properties segregate ETCs and TCs into distinct cell populations (Antal *et al.* 2006). Consistent with these lines of evidence, we observed no significant correlation between TC somatic depth and FI curve gain, peak instantaneous firing rate or firing regularity (Fig. S6). The results reported here thus define the fundamental intrinsic biophysical differences between MOB MCs and TCs.

References

Angelo K & Margrie TW (2011). Population diversity and function of hyperpolarization-activated current in olfactory bulb mitral cells. *Sci Rep* **1**, 50.

Angelo K, Rancz EA, Pimentel D, Hundahl C, Hannibal J, Fleischmann A, Pichler B & Margrie TW (2012). A biophysical signature of network affiliation and sensory processing in mitral cells. *Nature* **488**, 375–378.

Antal M, Eyre M, Finklea B & Nusser Z (2006). External tufted cells in the main olfactory bulb form two distinct subpopulations. *Eur J Neurosci* **24**, 1124–1136.

Arevian AC, Kapoor V & Urban NN (2008). Activity-dependent gating of lateral inhibition in the mouse olfactory bulb. *Nat Neurosci* **11**, 80–87.

Balu R, Larimer P & Strowbridge BW (2004). Phasic stimuli evoke precisely timed spikes in intermittently discharging mitral cells. *J Neurophysiol* **92**, 743–753.

Balu R, Pressler RT & Strowbridge BW (2007). Multiple modes of synaptic excitation of olfactory bulb granule cells. *J Neurosci* **27**, 5621–5632.

Bathellier B, Buhl DL, Accolla R & Carleton A (2008). Dynamic ensemble odor coding in the mammalian olfactory bulb: sensory information at different timescales. *Neuron* **57**, 586–598.

Bathellier B, Gschwend O & Carleton A (2010). Temporal coding in olfaction. In *The Neurobiology of Olfaction*, ed. Menini A, pp. 329–348. CRC Press, Boca Raton, FL.

Blauvelt DG, Sato TF, Wienisch M, Knöpfel T & Murthy VN (2013). Distinct spatiotemporal activity in principal neurons of the mouse olfactory bulb in anesthetized and awake states. *Front Neural Circuits* **7**, 46.

Boyd AM, Sturgill JF, Poo C & Isaacson JS (2012). Cortical feedback control of olfactory bulb circuits. *Neuron* **76**, 1161–1174.

Buonviso N, Amat C, Litaudon P, Roux S, Royet J-P, Farget V & Sicard G (2003). Rhythm sequence through the olfactory bulb layers during the time window of a respiratory cycle. *Eur J Neurosci* **17**, 1811–1819.

Burton SD, Ermentrout GB& Urban NN (2012). Intrinsic heterogeneity in oscillatory dynamics limits correlation-induced neural synchronization. *J Neurophysiol* **108**, 2115–2133.

Cajal SR (1911). *Histologie du système nerveux de l'homme et des vertébrés*, Vol. 2, pp. 891–942. Maloine, Paris.

Cang J & Isaacson JS (2003). *In vivo* whole-cell recording of odor-evoked synaptic transmission in the rat olfactory bulb. *J Neurosci* **23**, 4108–4116.

Carey RM & Wachowiak M (2011). Effect of sniffing on the temporal structure of mitral/tufted cell output from the olfactory bulb. *J Neurosci* **31**, 10615–10626.

Carlson GC, Shipley MT & Keller A (2000). Long-lasting depolarizations in mitral cells of the rat olfactory bulb. *J Neurosci* **20**, 2011–2021.

Chen WR & Shepherd GM (1997). Membrane and synaptic properties of mitral cells in slices of rat olfactory bulb. *Brain Res* **745**, 189–196.

Christie JM, Schoppa NE & Westbrook GL (2001). Tufted cell dendrodendritic inhibition in the olfactory bulb is dependent on NMDA receptor activity. *J Neurophysiol* **85**, 169–173.

Cury KM & Uchida N (2010). Robust odor coding via inhalation-coupled transient activity in the mammalian olfactory bulb. *Neuron* **68**, 570–585.

D'Souza RD & Vijayaraghavan S (2012). Nicotinic receptor-mediated filtering of mitral cell responses to olfactory nerve inputs involves the $\alpha 3\beta 4$ subtype. *J Neurosci* **32**, 3261–3266.

D'Souza RD, Parsa PV & Vijayaraghavan S (2013). Nicotinic receptors modulate olfactory bulb external tufted cells via an excitation-dependent inhibitory mechanism. *J Neurophysiol* **110**, 1544–1553.

De Saint Jan D, Hirnet D, Westbrook GL & Charpak S (2009). External tufted cells drive the output of olfactory bulb glomeruli. *J Neurosci* **29**, 2043–2052.

Del Punta K, Puche A, Adams NC, Rodriguez I & Mombaerts P (2002). A divergent pattern of sensory axonal projections is rendered convergent by second-order neurons in the accessory olfactory bulb. *Neuron* **35**, 1057–1066.

Desmaisons D, Vincent JD & Lledo PM (1999). Control of action potential timing by intrinsic subthreshold oscillations in olfactory bulb output neurons. *J Neurosci* **19**, 10727–10737.

Devore S & Linster C (2012). Noradrenergic and cholinergic modulation of olfactory bulb sensory processing. *Front Behav Neurosci* **6**, 52.

Ezeh PI, Wellis DP & Scott JW (1993). Organization of inhibition in the rat olfactory bulb external plexiform layer. *J Neurophysiol* **70**, 263–274.

Fadool DA, Tucker K & Pedarzani P (2011). Mitral cells of the olfactory bulb perform metabolic sensing and are disrupted by obesity at the level of the Kv1.3 ion channel. *PLoS ONE* **6**, e24921.

Fadool DA, Tucker K, Phillips JJ & Simmen JA (2000). Brain insulin receptor causes activity-dependent current suppression in the olfactory bulb through multiple phosphorylation of Kv1.3. *J Neurophysiol* **83**, 2332–2348.

Feng G, Mellor RH, Bernstein M, Keller-Peck C, Nguyen QT, Wallace M, Nerbonne JM, Lichtman JW & Sanes JR (2000). Imaging neuronal subsets in transgenic mice expressing multiple spectral variants of GFP. *Neuron* **28**, 41–51.

Friedman D & Strowbridge BW (2000). Functional role of NMDA autoreceptors in olfactory mitral cells. *J Neurophysiol* **84**, 39–50.

Friedrich RW (2006). Mechanisms of odor discrimination: neurophysiological and behavioral approaches. *Trends Neurosci* **29**, 40–47.

Fukunaga I, Berning M, Kollo M, Schmaltz A & Schaefer AT (2012). Two distinct channels of olfactory bulb output. *Neuron* **75**, 320–329.

Ghosh S, Larson SD, Hefzi H, Marnoy Z, Cutforth T, Dokka K & Baldwin KK (2011). Sensory maps in the olfactory cortex defined by long-range viral tracing of single neurons. *Nature* **472**, 217–220.

Gire DH & Schoppa NE (2009). Control of on/off glomerular signaling by a local GABAergic microcircuit in the olfactory bulb. *J Neurosci* **29**, 13454–13464.

Gire DH, Franks KM, Zak JD, Tanaka KF, Whitesell JD, Mulligan AA, Hen R & Schoppa NE (2012). Mitral cells in the olfactory bulb are mainly excited through a multistep signaling path. *J Neurosci* **32**, 2964–2975.

Giridhar S & Urban NN (2012). Mechanisms and benefits of granule cell latency coding in the mouse olfactory bulb. *Front Neural Circuits* **6**, 40.

Golomb D, Donner K, Shacham L, Shlosberg D, Amitai Y & Hansel D (2007). Mechanisms of firing patterns in fast-spiking cortical interneurons. *PLoS Comput Biol* **3**, e156.

Golowasch J, Thomas G, Taylor AL, Patel A, Pineda A, Khalil C & Nadim F (2009). Membrane capacitance measurements revisited: dependence of capacitance value on measurement method in nonisopotential neurons. *J Neurophysiol* **102**, 2161–2175.

Gracia-Llanes FJ, Crespo C, Blasco-Ibáñez JM, Nácher J, Varea E, Rovira-Esteban L & Martínez-Guijarro FJ (2010). GABAergic basal forebrain afferents innervate selectively GABAergic targets in the main olfactory bulb. *Neuroscience* **170**, 913–922.

Griff ER, Mafhouz M & Chaput MA (2008). Comparison of identified mitral and tufted cells in freely breathing rats: II. Odor-evoked responses. *Chem Senses* **33**, 793–802.

Haddad R, Lanjuin A, Madisen L, Zeng H, Murthy VN & Uchida N (2013). Olfactory cortical neurons read out a relative time code in the olfactory bulb. *Nat Neurosci* **16**, 949–957.

Hayar A, Karnup S, Shipley MT & Ennis M (2004). Olfactory bulb glomeruli: external tufted cells intrinsically burst at theta frequency and are entrained by patterned olfactory input. *J Neurosci* **24**, 1190–1199.

Holt GR, Softky WR, Koch C & Douglas RJ (1996). Comparison of discharge variability in vitro and in vivo in cat visual cortex neurons. *J Neurophysiol* **75**, 1806–1814.

Huang L, Garcia I, Jen HI& Arenkiel BR (2013). Reciprocal connectivity between mitral cells and external plexiform layer interneurons in the mouse olfactory bulb. *Front Neural Circuits* **7**, 32.

Igarashi KM, Ieki N, An M, Yamaguchi Y, Nagayama S, Kobayakawa K, Kobayakawa R, Tanifuji M, Sakano H, Chen WR & Mori K (2012). Parallel mitral and tufted cell pathways route distinct odor information to different targets in the olfactory cortex. *J Neurosci* **32**, 7970–7985.

Kato HK, Chu MW, Isaacson JS & Komiyama T (2012). Dynamic sensory representations in the olfactory bulb: modulation by wakefulness and experience. *Neuron* **76**, 962–975.

Kato HK, Gillet SN, Peters AJ, Isaacson JS & Komiyama T (2013). Parvalbumin-expressing interneurons linearly control olfactory bulb output. *Neuron* **80**, 1218–1231.

Kikuta S, Fletcher ML, Homma R, Yamasoba T & Nagayama S (2013). Odorant response properties of individual neurons in an olfactory glomerular module. *Neuron* **77**, 1122–1135.

King JD & Meriney SD (2005). Proportion of N-type calcium current activated by action potential stimuli. *J Neurophysiol* **94**, 3762–3770.

Kishi K, Mori K & Ojima H (1984). Distribution of local axon collaterals of mitral, displaced mitral, and tufted cells in the rabbit olfactory bulb. *J Comp Neurol* **225**, 511–526.

Labarrera C, London M & Angelo K (2013). Tonic inhibition sets the state of excitability in olfactory bulb granule cells. *J Physiol* **591**, 1841–1850.

Liu S & Shipley MT (2008). Multiple conductances cooperatively regulate spontaneous bursting in mouse olfactory bulb external tufted cells. *J Neurosci* **28**, 1625–1639.

Livneh Y, Adam Y & Mizrahi A (2014). Odor processing by adult-born neurons. *Neuron* **81**, 1097–1110.

Ma JJ & Lowe GG (2010). Correlated firing in tufted cells of mouse olfactory bulb. *Neuroscience* **169**, 1715–1738.

Ma M & Luo M (2012). Optogenetic activation of basal forebrain cholinergic neurons modulates neuronal excitability and sensory responses in the main olfactory bulb. *J Neurosci* **32**, 10105–10116.

Macrides F & Schneider SP (1982). Laminar organization of mitral and tufted cells in the main olfactory bulb of the adult hamster. *J Comp Neurol* **208**, 419–430.

Macrides F, Schoenfeld TA, Marchand JE & Clancy AN (1985). Evidence for morphologically, neurochemically and functionally heterogeneous classes of mitral and tufted cells in the olfactory bulb. *Chem Senses* **10**, 175–202.

Margrie TW & Schaefer AT (2003). Theta oscillation coupled spike latencies yield computational vigour in a mammalian sensory system. *J Physiol* **546**, 363–374.

Margrie TW, Sakmann B & Urban NN (2001). Action potential propagation in mitral cell lateral dendrites is decremental and controls recurrent and lateral inhibition in the mammalian olfactory bulb. *Proc Natl Acad Sci U S A* **98**, 319–324.

Markopoulos F, Rokni D, Gire DH & Murthy VN (2012). Functional properties of cortical feedback projections to the olfactory bulb. *Neuron* **76**, 1175–1188.

Markram H, Toledo-Rodriguez M, Wang Y, Gupta A, Silberberg G & Wu C (2004). Interneurons of the neocortical inhibitory system. *Nat Rev Neurosci* **5**, 793–807.

McGann JP (2013). Presynaptic inhibition of olfactory sensory neurons: new mechanisms and potential functions. *Chem Senses* **38**, 459–474.

Migliore M & Shepherd GM (2002). Emerging rules for the distributions of active dendritic conductances. *Nat Rev Neurosci* **3**, 362–370.

Miyamichi K, Shlomai-Fuchs Y, Shu M, Weissbourd BC, Luo L & Mizrahi A (2013). Dissecting local circuits: parvalbumin interneurons underlie broad feedback control of olfactory bulb output. *Neuron* **80**, 1232–1245.

Mori K & Sakano H (2011). How is the olfactory map formed and interpreted in the mammalian brain? *Annu Rev Neurosci* **34**, 467–499.

Mori K, Kishi K & Ojima H (1983). Distribution of dendrites of mitral, displaced mitral, tufted, and granule cells in the rabbit olfactory bulb. *J Comp Neurol* **219**, 339–355.

Nagayama S, Enerva A, Fletcher ML, Masurkar AV, Igarashi KM, Mori K & Chen WR (2010). Differential axonal projection of mitral and tufted cells in the mouse main olfactory system. *Front Neural Circuits* **4**, 120.

Nagayama S, Takahashi YK, Yoshihara Y & Mori K (2004). Mitral and tufted cells differ in the decoding manner of odor maps in the rat olfactory bulb. *J Neurophysiol* **91**, 2532–2540.

Najac M, De Saint Jan D, Reguero L, Grandes P & Charpak S (2011). Monosynaptic and polysynaptic feed-forward inputs to mitral cells from olfactory sensory neurons. *J Neurosci* **31**, 8722–8729.

Nunez-Parra A, Maurer RK, Krahe K, Smith RS & Araneda RC (2013). Disruption of centrifugal inhibition to olfactory bulb granule cells impairs olfactory discrimination. *Proc Natl Acad Sci U S A* **110**, 14777–14782.
Orona E, Rainer EC & Scott JW (1984). Dendritic and axonal organization of mitral and tufted cells in the rat olfactory bulb. *J Comp Neurol* **226**, 346–356.
Oswald A-M & Urban NN (2012*a*). There and back again: the corticobulbar loop. *Neuron* **76**, 1045–1047.
Oswald A-MM & Urban NN (2012*b*). Interactions between behaviorally relevant rhythms and synaptic plasticity alter coding in the piriform cortex. *J Neurosci* **32**, 6092–6104.
Padmanabhan K & Urban NN (2010). Intrinsic biophysical diversity decorrelates neuronal firing while increasing information content. *Nat Neurosci* **13**, 1276–1282.
Parrish-Aungst S, Shipley MT, Erdelyi F, Szabo G & Puche AC (2007). Quantitative analysis of neuronal diversity in the mouse olfactory bulb. *J Comp Neurol* **501**, 825–836.
Patterson MA, Lagier S & Carleton A (2013). Odor representations in the olfactory bulb evolve after the first breath and persist as an odor afterimage. *Proc Natl Acad Sci U S A* **110**, E3340–E3349.
Petzold GC, Hagiwara A & Murthy VN (2009). Serotonergic modulation of odor input to the mammalian olfactory bulb. *Nat Neurosci* **12**, 784–791.
Phillips ME, Sachdev RNS, Willhite DC & Shepherd GM (2012). Respiration drives network activity and modulates synaptic and circuit processing of lateral inhibition in the olfactory bulb. *J Neurosci* **32**, 85–98.
Potter SM, Zheng C, Koos DS, Feinstein P, Fraser SE & Mombaerts P (2001). Structure and emergence of specific olfactory glomeruli in the mouse. *J Neurosci* **21**, 9713–9723.
Rinzel J & Ermentrout GB (1989). Analysis of neural excitability and oscillations. In *Methods in Neuronal Modeling*, eds Koch C & Segev I, pp. 135–169. MIT Press, Cambridge, MA.
Rush ME & Rinzel J (1995). The potassium A-current, low firing rates and rebound excitation in Hodgkin–Huxley models. *Bull Math Biol* **57**, 899–929.
Schaefer AT & Margrie TW (2007). Spatiotemporal representations in the olfactory system. *Trends Neurosci* **30**, 92–100.
Schaefer AT & Margrie TW (2012). Psychophysical properties of odor processing can be quantitatively described by relative action potential latency patterns in mitral and tufted cells. *Front Syst Neurosci* **6**, 30.
Schaefer AT, Angelo K, Spors H & Margrie TW (2006). Neuronal oscillations enhance stimulus discrimination by ensuring action potential precision. *PLoS Biol* **4**, e163.
Schneider SP & Scott JW (1983). Orthodromic response properties of rat olfactory bulb mitral and tufted cells correlate with their projection patterns. *J Neurophysiol* **50**, 358–378.
Schoppa NE (2006). Synchronization of olfactory bulb mitral cells by precisely timed inhibitory inputs. *Neuron* **49**, 271–283.
Schoppa NE & Urban NN (2003). Dendritic processing within olfactory bulb circuits. *Trends Neurosci* **26**, 501–506.
Schoppa NE & Westbrook GL (2002). AMPA autoreceptors drive correlated spiking in olfactory bulb glomeruli. *Nat Neurosci* **5**, 1194–1202.
Shao Z, Puche AC & Shipley MT (2013). Intraglomerular inhibition maintains mitral cell response contrast across input frequencies. *J Neurophysiol* **110**, 2185–2191.
Shao Z, Puche AC, Liu S & Shipley MT (2012). Intraglomerular inhibition shapes the strength and temporal structure of glomerular output. *J Neurophysiol* **108**, 782–793.
Shusterman R, Smear MC, Koulakov AA & Rinberg D (2011). Precise olfactory responses tile the sniff cycle. *Nat Neurosci* **14**, 1039–1044.
Smear M, Resulaj A, Zhang J, Bozza T & Rinberg D (2013). Multiple perceptible signals from a single olfactory glomerulus. *Nat Neurosci* **16**, 1687–1691.
Stiefel KM, Englitz B & Sejnowski TJ (2013). Origin of intrinsic irregular firing in cortical interneurons. *Proc Natl Acad Sci U S A* **110**, 7886–7891.
Tepper JMJ & Bolam JPJ (2004). Functional diversity and specificity of neostriatal interneurons. *Curr Opin Neurobiol* **14**, 685–692.
Tripathy SJ, Padmanabhan K, Gerkin RC & Urban NN (2013). Intermediate intrinsic diversity enhances neural population coding. *Proc Natl Acad Sci U S A* **110**, 8248–8253.
Tucker K & Fadool DA (2002). Neurotrophin modulation of voltage-gated potassium channels in rat through TrkB receptors is time and sensory experience dependent. *J Physiol* **542**, 413–429.
Tucker K, Cho S, Thiebaud N, Henderson MX & Fadool DA (2013). Glucose sensitivity of mouse olfactory bulb neurons is conveyed by a voltage-gated potassium channel. *J Physiol* **591**, 2541–2561.
Urban NN & Sakmann B (2002). Reciprocal intraglomerular excitation and intra- and interglomerular lateral inhibition between mouse olfactory bulb mitral cells. *J Physiol* **542**, 355–367.
Wachowiak M (2011). All in a sniff: olfaction as a model for active sensing. *Neuron* **71**, 962–973.
Wachowiak M, Economo MN, Díaz-Quesada M, Brunert D, Wesson DW, White JA & Rothermel M (2013). Optical dissection of odor information processing in vivo using GCaMPs expressed in specified cell types of the olfactory bulb. *J Neurosci* **33**, 5285–5300.
Wellis DP, Scott JW & Harrison TA (1989). Discrimination among odorants by single neurons of the rat olfactory bulb. *J Neurophysiol* **61**, 1161–1177.

Additional Information

Competing interests

The authors declare no conflict of interest.

Author contributions

All experiments were performed in the laboratory of N.N.U. at Carnegie Mellon University. S.D.B. and N.N.U. designed the research; S.D.B. performed the research; S.D.B. and N.N.U.

analysed the data; S.D.B. and N.N.U. wrote the manuscript; S.D.B. and N.N.U. approved the final version of the manuscript.

Funding

This work was supported by an Achievement Rewards for College Scientists Foundation fellowship (S.D.B.) and National Institute on Deafness and Other Communication Disorders grants F31DC013490 (S.D.B.) and R01DC005798 (N.N.U.).

Acknowledgements

We thank Greg LaRocca and Jennifer Dry-Henich for excellent technical assistance and members of the Urban, Oswald and Kuhlman laboratories for helpful discussions.

Supporting Information

The following supporting information is available in the online version of this article.

Figure S1. MC morphology.
Figure S2. TC morphology.
Figure S3. MC and TC intrinsic biophysical properties are largely independent of morphological properties.
Figure S4. The diversity of afferent-evoked firing modes is predicted by somatic step current injections.
Figure S5. Biophysical diversity within MCs and TCs is largely independent of age.
Figure S6. Depth analysis of TCs.